The Astrophysical Journal, 895:21 (18pp), 2020 May 20 https://doi.org/10.3847/1538-4357/ab8883

ALMA Observations of the Molecular Clouds in NGC 625

Nia Imara[1], Ilse De Looze[2,3], Christopher M. Faesi[1,4], and Diane Cormier[5]
[1] Harvard-Smithsonian Center for Astrophysics, 60 Garden Street, Cambridge, MA 02138, USA; nimara@cfa.harvard.edu
[2] Sterrenkundig Observatorium, Universiteit Gent, Krijgslaan 281 S9, B-9000 Gent, Belgium
[3] Department of Physics and Astronomy, University College London, Gower Street, London WC1E 6BT, UK
[4] University of Massachusetts—Amherst, 710 N. Pleasant Street, Amherst, MA 01003, USA
[5] AIM, CEA, CNRS, Université Paris-Saclay, Université Paris Diderot, Sorbonne Paris Cité, F-91191 Gif-sur-Yvette, France
Received 2019 May 6; revised 2020 March 25; accepted 2020 April 3; published 2020 May 20

Abstract

We present the highest-resolution (1″) ^{12}CO observations of molecular gas in the dwarf starburst galaxy NGC 625 to date, obtained with Atacama Large Millimeter/submillimeter Array. The molecular gas, which is distributed in discrete clouds within an area of 0.4 kpc^2, does not have well-ordered large-scale motions. We measure a molecular mass in NGC 625 of 5.3×10^6 $M_\odot$, assuming a Milky Way CO-to-H_2 conversion factor. We use the CPROPS package to identify molecular clouds and measure their properties. The 19 resolved CO clouds have a median radius of 20 pc, a median linewidth 2.5 km s^{-1}, and a median surface density of 169 $M_\odot$ pc^{-2}. Larson scaling relations suggest that molecular clouds in NGC 625 are mostly in virial equilibrium. Comparison of our high-resolution CO observations with a star formation rate map, inferred from ancillary optical observations, suggests that about 40% of the molecular clouds coincide with the brightest H II regions. These bright H II regions have a range of molecular gas depletion timescales, all within a factor of ∼3 of the global depletion time in NGC 625 of 106–134 Myr. The highest surface density molecular clouds toward the southwest of the galaxy, in a region we call the Butterfly, do not show strong star formation activity and suggest a depletion timescale longer than 5 Gyr.

Unified Astronomy Thesaurus concepts: Dwarf galaxies (416); Galaxies (573); Star formation (1569); Interstellar medium (847); Giant molecular clouds (653); Molecular gas (1073); Interstellar molecules (849); Starburst galaxies (1570); Metallicity (1031); Interferometry (808); Submillimeter astronomy (1647); Molecular clouds (1072)

1. Introduction

Nearby star-forming dwarf galaxies present a wonderful opportunity for studying the initial conditions of star formation in environments different from the Milky Way. With their intense radiation fields, low metal abundances, high gas-to-dust ratios, low masses, and shallow potential wells, the conditions in the interstellar medium (ISM) of dwarf galaxies (e.g., Kunth & Östlin 2000; Madden et al. 2006; Draine et al. 2007) may affect the properties of giant molecular clouds (GMCs), the sites of most star formation (e.g., Bolatto et al. 2013). Moreover, nearby dwarf galaxies are useful laboratories to investigate early universe star formation that occurred in low-metallicity environments.

A question at the heart of star formation research is how the properties of GMCs—properties including size, mass, velocity dispersion, and surface density—vary across galactic environment (e.g., Fukui & Kawamura 2010). On a related issue, we would like to understand whether and how galactic environment affects the distribution of and correlation between the physical properties of GMCs. A consensus on the key environmental factors driving differences in cloud character has not been reached. This is in part due to inhomogeneous data sets used to make comparisons between cloud populations; in part due to our incomplete knowledge of quantities like the CO-to-H_2 conversion factor, which must be assumed in order to estimate luminous masses for clouds, which are composed primarily of molecular hydrogen, H_2. In low-metallicity galaxies, the CO luminosity tends to be faint. The intense radiation fields combined with suppressed dust shielding may lead to the dissociation of molecules at a quicker rate, and the formation of H_2 on dust grains is expected to be curbed (e.g., Wolfire et al. 2010). Moreover, because the CO molecule is more susceptible to dissociating UV radiation compared to H_2, the CO-emitting regions of molecular clouds in these environments may be smaller and the CO-to-H_2 conversion factor higher (e.g., Arimoto et al. 1996; Israel 1997; Boselli et al. 2002; Imara & Blitz 2007; Leroy et al. 2011; Schruba et al. 2012; Bolatto et al. 2013; Cormier et al. 2014; Hunt et al. 2015; Amorín et al. 2016).

In recent years, wide-field and high-resolution observations of the molecular ISM have become increasingly available, furthering our knowledge of resolved, extragalactic molecular clouds (e.g., Bolatto et al. 2008; Fukui et al. 2008; Wong et al. 2011; Leroy et al. 2015; Rubio et al. 2015; Kepley et al. 2016; Schruba et al. 2017; Faesi et al. 2018; Imara & Faesi 2019). These studies have demonstrated that, although some cloud properties and scaling relations are similar across environments, those in dwarf and starburst galaxies often display considerable differences from their counterparts in massive disk galaxies (e.g., Leroy et al. 2015; Kepley et al. 2016; Imara & Faesi 2019). Our understanding of the contrasts between star-forming gas in starburst dwarf galaxies and disks is particularly limited, as only a handful of these former systems have been observed at sufficiently high resolution and sensitivity to acquire large number statistics of their cloud populations (e.g., Leroy et al. 2015; Kepley et al. 2016; Miura et al. 2018; Imara & Faesi 2019).

Blue compact dwarf (BCD) galaxies—faint, compact objects with high star formation rates (SFR) relative to their masses—have been proposed as good analogs for starburst systems in

Table 1
Properties of NGC 625

Property	Value	Reference
Distance	3.9 Mpc	1
Absolute B magnitude	−16.2	2
Metallicity	$12 + \log(\mathrm{O/H}) = 8.22$	3
Size (D_{25})	$5\farcm8 \times 1\farcm9$	4
Stellar mass	$3.0 \times 10^8 M_\odot$	4
FIR luminosity	$2.6 \times 10^8\ L_\odot$	4
$\mathrm{SFR_{FIR}}$	$0.04\ M_\odot\ \mathrm{yr}^{-1}$	4
$\mathrm{SFR_{H\alpha}}$	$0.05\ M_\odot\ \mathrm{yr}^{-1}$	3
Inclination	65°	5
H I mass	$(1.1 \pm 0.2) \times 10^8 M_\odot$	5
H_2 mass (single-dish)	$(5.0 \pm 0.7) \times 10^6\ M_\odot$	6
H_2 mass (ALMA)	$(5.34 \pm 0.34) \times 10^6\ M_\odot$	This work
Molecular depletion time	106–134 Myr	This work

References. (1) Cannon et al. 2003; (2) de Vaucouleurs et al. 1991; (3) Skillman et al. 2003a; (4) Madden et al. 2013; (5) Cannon et al. 2004; (6) Cormier et al. 2014.

the early universe (e.g., Leroy et al. 2015; Miura et al. 2018). What drives the differences between molecular clouds in these environments and in disks, and how star formation is triggered in starbursts, are questions under active investigation. Atacama Large Millimeter/Submillimeter Array (ALMA) observations of the BCD galaxy II Zw 40 revealed clumpy molecular gas characterized by larger linewidths and higher cloud surface densities compared to molecular clouds in disk galaxies (Kepley et al. 2016). More recently, Imara & Faesi (2019) observed the BCD Henize 2–10 with ALMA, showing that while the surface densities of GMCs in this galaxy are similar to those of Milky Way clouds, the average molecular gas surface density of the BCD *as a whole* is a factor of 30–70 higher than in the Milky Way disk, reflecting the fact that the molecular gas filling factor in Henize 2–10 is close to unity. The studies of II Zw 40 and Henize 2–10 represent only a small number of existing millimeter observations of BCDs that are available to investigate GMC properties in these extreme environments.

We present new ^{12}CO ($J = 1 - 0$) ALMA observations of the BCD NGC 625, a relatively isolated, gas-rich galaxy in the Sculptor Group, at a distance of 3.89 ± 0.22 Mpc (Cannon et al. 2003). NGC 625 has a metallicity of $12 + \log(\mathrm{O/H}) = 8.22$ ($\approx 1/3 Z_\odot$; Skillman et al. 2003a).[6] The galaxy is one of the few known dwarfs with a large-scale, high-velocity H I outflow, which may be a consequence of its prolonged, ∼100 Myr episode of star formation (Cannon et al. 2004, 2005). The stellar mass of NGC 625 ($3 \times 10^8 M_\odot$; Madden et al. 2013) and its atomic hydrogen mass ($1.1 \times 10^8 M_\odot$; Cannon et al. 2004) are comparable to those of IC 10 (see Table 1). Single-dish CO observations of NGC 625 were reported by Cormier et al. (2014), who found a total molecular gas mass of $5 \times 10^6\ M_\odot$, assuming a Galactic CO-to-H_2 conversion factor. Its current SFR of $0.05\ M_\odot\ \mathrm{yr}^{-1}$ is similar to that of the Small Magellanic Cloud (SMC), although its gas depletion time of ∼2 Gyr may be twice as long as that in the SMC (Skillman et al. 2003a).

Our main goals in this study are to present the new data, to describe the global properties of the molecular gas as inferred from the CO observations, and to identify and characterize the properties of molecular clouds in NGC 625. To explore how differences in galactic environment—particularly in starburst dwarf galaxies—influence the properties of molecular clouds, we will examine how empirical relationships determined for NGC 625 molecular clouds compare with general trends observed in the Milky Way and external galaxies. Finally, we will investigate the relationship between GMCs and star formation activity as inferred from Hα observations. In Section 2, we provide an overview of our ALMA observations, the highest resolution to date of NGC 625, and we describe the Hα observations to which we later compare the distribution of molecular gas. In Section 3, we describe the global properties of the molecular gas. In Section 4, we identify and characterize the properties of GMCs in NGC 625, and we compare them to trends observed for molecular clouds in other galaxies. We discuss the relationship between GMCs and H II regions in Section 5, and in Section 6 we discuss the star formation efficiency (SFE) in NGC 625. We summarize our conclusions in Section 7.

2. Observations

2.1. New ALMA CO Observations

We obtained ALMA Cycle 3 observations (project code 2015.1.01395.S; PI: Nia Imara) in the ^{12}CO(1–0) line at 115.2712 GHz toward NGC 625 in 2016 May. Two positions were observed that covered the optical nucleus of the galaxy. The overlapping beams had a phase center of $01^h35^m06\overset{s}{.}90$, $-41°26'13\farcs47$ [J2000], and the center of the beams was separated by half the half-power beamwidth (∼25″). The ALMA 12 m array was in configuration C36-3 for the five observing nights, with 36 antennas every night, arranged with baselines from 15 to 639 m, implying a minimum angular resolution of ∼1.″1 and a maximum recoverable scale of ∼10.″7 (at 115.27 GHz). The half-power beamwidth for the 12 m array was 50.″7. Table 2 summarizes the observing dates, conditions, and calibrators.

The ALMA Band 3 correlator was set up to have a velocity resolution of 564.453 kHz (1.470 km s^{-1}) and a bandwidth of 937.50 MHz, centered at 114.936 GHz to cover the ^{12}CO(1–0) line, adjusted for the galaxy's LSR velocity of 395 km s^{-1}. We also observed continuum by centering the remaining basebands at 102, 101, and 113 GHz, each with bandwidths of 1.875 GHz.

Our data were processed and imaged using the Common Astronomy Software Applications (CASA) package (https://casa.nrao.edu). The North American ALMA Science team used CASA version 4.5.3 to manually calibrate the data. We summarize the data processing steps as follows. First, there were basic flagging operations, including autocorrelation, shadowed antenna, and edge channel flagging. Next, a system temperature (T_{sys}) calibration table was generated and deviant T_{sys} measurements were flagged. Then the antenna positions were calibrated, followed by atmospheric calibration using the Water Vapor Radiometer data. Finally, the bandpass, flux, and gain calibrations were performed.

We imaged our data in CASA using the `multiscale` CLEAN algorithm. This method, which searches for emission at a range of spatial scales, has been shown to do well at recovering extended emission, reducing the depth of negative emission features, and eliminating low-level flux missed by standard CLEAN algorithms, which only clean point-source–scale emission

[6] We assume a solar oxygen abundance of $12 + \log(\mathrm{O/H}) = 8.69$ (Asplund et al. 2009).

Table 2
Observation Summary

Date	2016 May 3	2016 May 7	2016 May 7	2016 May 8	2016 May 8
On-source time	48.12 minutes	48.15 minutes	48.12 minutes	48.13 minutes	48.13
Number of Antennas	36	36	36	36	36
Average T_{sys}	120.6 K	128.7 K	142.6 K	123.2 K	160.0 K
Mean precipitable water vapor	2.73 mm	2.90 mm	3.07 mm	2.35 mm	2.97 mm
Bandpass calibrator	J2357-5311	J2357-5311	J2357-5311	J2357-5311	J0334-4088
Flux calibrator	Neptune	J2357-5311	J0334-4008	J2357-5311	J0334-4088
Phase calibrator	J0136-4044	J0136-4044	J0136-4044	J0136-4044	J0136-4044
Pointing calibrators	J0134-3843, J2357-5311, J2246-1206	J2357-5311	J2357-5311, J0334-4008	J2357-5311	J0334-4088

(e.g., Rich et al. 2008). With the aim of measuring the CO-derived properties of molecular clouds, natural weighting was chosen in order to maximize sensitivity. We imaged the continuum emission, detected a total flux of about 4 mJy, and subtracted this from the line emission.

Our process for imaging the CO line took several steps: first, we examined each of the 101 (1.5 km s^{-1} wide) velocity channels around the systemic velocity of NGC 625 to determine where significant emission is arising. Next, a mask was drawn around all the significant and coherent emission. This mask was then used to deconvolve all image planes. The deconvolution was stopped when the cumulative flux as a function of the number of CLEAN iterations converged. We confirmed that the deconvolution was satisfactory by confirming that the residual data cube looked like noise. We performed a third check by repeating the deconvolution process, this time with double the number of CLEAN iterations, and subtracting the resulting deconvolved cubes from the previous results to again confirm that it looked like noise.

Finally, we applied a primary beam correction, using the combined beam pattern of the two pointings, though we note that since most of the emission is concentrated in the central portion of the image, the effect on our measured flux is minimal. The final data cube has voxels with dimensions of $0\farcs25 \times 0\farcs25 \times 1.5$ km s^{-1} and a spatial extent of $1\farcm25$. The synthesized beam was measured to be $1\farcs31 \times 1\farcs08$, corresponding to a spatial resolution of 24.6 pc × 20.3 pc at the distance to NGC 625. The rms sensitivity is 10.3 mJy per 1.5 km s^{-1} channel. The corresponding rms brightness temperature is 0.7 K per channel. For a typical molecular cloud linewidth of ∼3 km s^{-1} (i.e., two channels), this yields an rms integrated intensity of ∼2 K km s^{-1}. Assuming a Galactic CO-to-H_2 conversion factor of 4.35 $M_\odot$ (K km s^{-1} pc^2)$^{-1}$ (see Section 3.1 below; Dame et al. 2001; Bolatto et al. 2013), the corresponding 5σ sensitivity limit of the mass surface density is 43 $M_\odot$ pc^{-2}.

Interferometric observations without zero- or short-spacing data inevitably miss flux, particularly extended emission, from the observed source. We did not have total power observations, and so we examined the impact of imaging the data with tapered visibilities on flux recovery. We repeated the deconvolution process using tapered visibility (uv) weights, which effectively increases the surface brightness sensitivity at the cost of angular resolution. There are, however, limits to tapering in the uv plane, because the overall sensitivity will decrease as the data are increasingly downweighted and information at small spatial scales is lost. We used Gaussian taper functions that yielded final resolutions of roughly 3″ and 6″. The rms noise levels of the 3″ and 6″ data cubes are 15.0 mJy per 3″ beam and 26.4 mJy per 6″ beam, respectively.

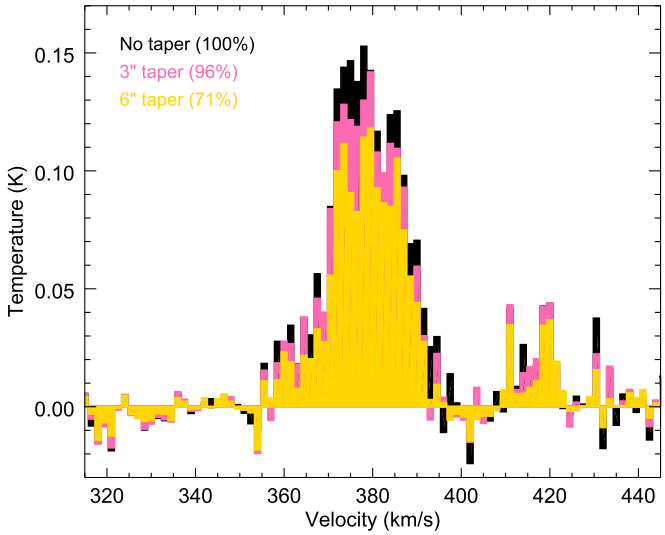

Figure 1. Composite ^{12}CO spectra of NGC 625. Black, pink, and gold spectra correspond to data cubes imaged at roughly 1″, 3″, and 6″, respectively. Top left corner lists the percentage of flux recovered, with respect to the 1″ cube.

Figure 1 displays the flux recovered by the CLEAN algorithm for the three different data cubes. The high-resolution, ∼1″ cube does not miss any significant amount of flux, while the 3″ cube captures 96% of the total flux, and the 6″ cube captures 71% of the total flux, with respect to the high-resolution cube. Although the tapered cubes recovered flux at extended spatial scales, they suppressed enough information at small scales that the overall recovered flux was less than that in the high-resolution cube. This suggests that our observations have not suffered significant spatial filtering. This agrees with our findings, discussed in Section 3.1, that our ALMA observations have a total ^{12}CO luminosity comparable to that of previous single-dish data obtained with the Australia Telescope National Facility (ATNF) Mopra 22 m telescope by Cormier et al. (2014).

Figure A1 in the Appendix shows an optical image of NGC 625 with our observed positions indicated by circles. Figure A2, also in the Appendix, displays the ALMA CO(1–0) peak flux map.

2.2. Archival Hubble Hα Observations

In Sections 5 and 6, we compare the distribution of molecular gas to Hα observations probing recent star formation activity. NGC 625 was observed with the Wide Field Planetary Camera 2 on the Hubble Space Telescope (HST) by Cannon et al. (2003). We retrieved images from the Hubble Legacy Archive in four passbands, including narrowband images of

Hα (F656N filter) and Hβ (F487N filter), and broadband images in the visible (F555W filter) and near-infrared (F814W filter). These Hubble images were (manually) corrected for astrometry offsets (with a final accuracy of ∼0.″1 for the astrometry) based on a comparison with the astrometry of stars in the NOMAD catalog, and then flux calibrated based on the PHOTFLAM keyword in the respective headers of the images.

To obtain continuum-subtracted Hα and Hβ maps, we first subtracted the combined Hα and Hβ emission (with a contribution of only a few percent) from the F555W continuum map, until no diffuse extended emission was visible in the F555W map and the morphology was similar to the line-free F814W continuum map, following the strategy suggested by Cannon et al. (2002, 2003). The line-free F555W map was subsequently used to obtain continuum-subtracted narrowband Hα and Hβ line maps.

The images were corrected for Galactic extinction following the reddening $E(B-V) = 0.16$ mag reported by Schlegel et al. (1998), assuming a Galactic dust extinction law. We applied the Balmer decrement (i.e., the ratio of the Hα/Hβ lines) to correct for internal dust extinction, following Kreckel et al. (2013). Due to the low signal-to-noise of the Hβ line, the internal dust extinction correction was mostly restricted to the two brightest H II regions (called A and B in the nomenclature of Cannon et al. 2003) with high Hα and Hβ equivalent width (Cannon et al. 2003). Based on the peak of MIPS 24 μm emission in those two brightest H II regions (see Figure A3 in the Appendix), and the weak mid-infrared emission originating from other parts of NGC 625, we argue that the dust extinction correction can be considered negligible outside of these two H II regions.

Theoretically, the (unobscured) Hα/Hβ ratio is equal to 2.86, under the assumption of Case B recombination, a gas temperature of $T = 10{,}000$ K, and electron density $n_e = 100\,\mathrm{cm}^{-3}$ (Osterbrock 1989). On average, we find Hα/Hβ ratios of 3.7 and 3.6 in the brightest H II regions A and B, but there is quite some variation throughout both regions. From these Hα/Hβ ratios, we infer an average V-band dust extinction of $A_V = 0.7$ and 0.6 for H II regions A and B, respectively. Our measured dust extinction is consistent with the A_V values of around 0.5 quoted in Cannon et al. (2003) for these two regions.

We infer the SFR in an ellipse, with semimajor axis of 20″ and semiminor axis of 14″, covering all the regions with detected Hα emission. The total SFR ($=0.05\,M_\odot$ yr^{-1}) we measure from the Hα map after correcting for dust extinction is in excellent agreement with the SFR estimate from Cannon et al. (2003).

We did not correct for possible N II contamination in the H II emission. In the star-forming regions of disk galaxies, at least, there is evidence that the N II flux is negligible (e.g., James et al. 2005). In particular for NGC 625, Skillman et al. (2003b) showed that the nitrogen abundance is very low, and that an uncertainty of about 6% is introduced to the Hα fluxes by not correcting them for possible N II contamination. Nevertheless, if N II emission is present in non-negligible amounts in the regions we investigate in NGC 625, we may slightly overestimate SFRs.

2.3. Archival Dust Continuum Observations

We retrieved the Spitzer MIPS 24 observations from Bendo et al. (2012), while Herschel SPIRE 250, 350, and 500 μm Level 2 data products were downloaded from the IRSA Herschel Science Archive.

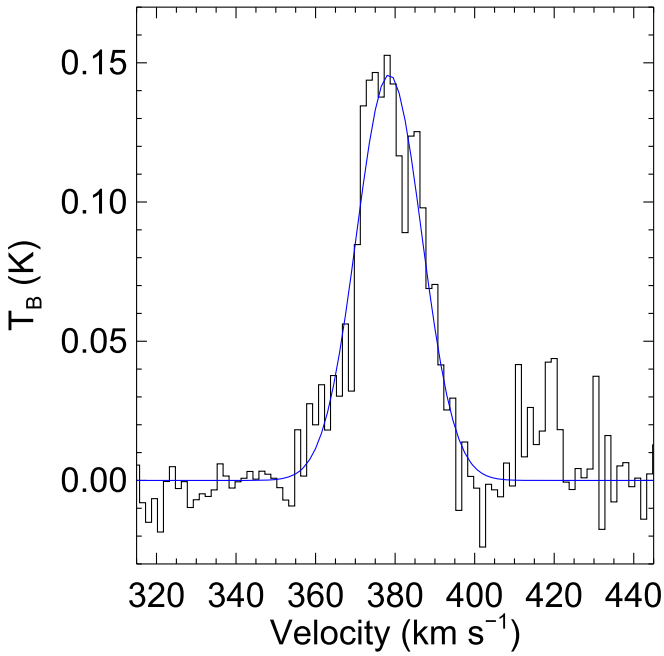

Figure 2. Composite ^{12}CO ALMA spectrum of NGC 625 (black) with a Gaussian fit (blue).

3. Global Properties of Molecular Gas

3.1. Integrated Intensity

In Figure 2, we display the observed integrated ^{12}CO(1–0) spectrum of NGC 625 in units of brightness temperature, T_B, created by averaging T_B across the image of the galaxy (displayed in Figure 3) in each channel. We fit a Gaussian to the spectrum, and we measure a peak temperature of 146 ± 6 mK occurring at a systematic central velocity of 378.5 km s^{-1}. The fit gives a gas velocity dispersion of (8.20 ± 0.38) km s^{-1}, yielding a total integrated CO intensity of $I_{CO} = (3.00 \pm 0.19)$ K km s^{-1}.

Cormier et al. (2014) reported single-dish CO(1–0) observations obtained with the ATNF Mopra 22 m telescope over the central part of NGC 625. They covered the galaxy with four overlapping pointings with a beam size of 30″ corresponding to an area of ≃0.9 kpc^2. They found a luminosity of $(1.1 \pm 0.2) \times 10^6$ K km s^{-1} pc^2, and a molecular gas mass of $(5.0 \pm 0.7) \times 10^6\,M_\odot$, assuming a Galactic conversion factor. While the Mopra observations are not as sensitive as the ALMA observations, Cormier et al. (2014) made measurements on the stacked spectra of the four positions observed with Mopra. These four positions roughly correspond to the area over which we measure the average CO spectrum with our ALMA data. The values obtained by Cormier et al. (2014) are in good agreement with our total values, suggesting that our interferometric data have not suffered from significant spatial filtering.

Figure 3 displays the ^{12}CO integrated intensity map, integrated over the velocity range 350–435 km s^{-1}. The size of the region is 57.″5 × 20″, corresponding to an area of 0.4 kpc^2 at the distance to the galaxy. Given the total integrated CO intensity we measure, the luminosity of this region is 1.2×10^6 K km s^{-1} pc^2. This is consistent with the luminosity

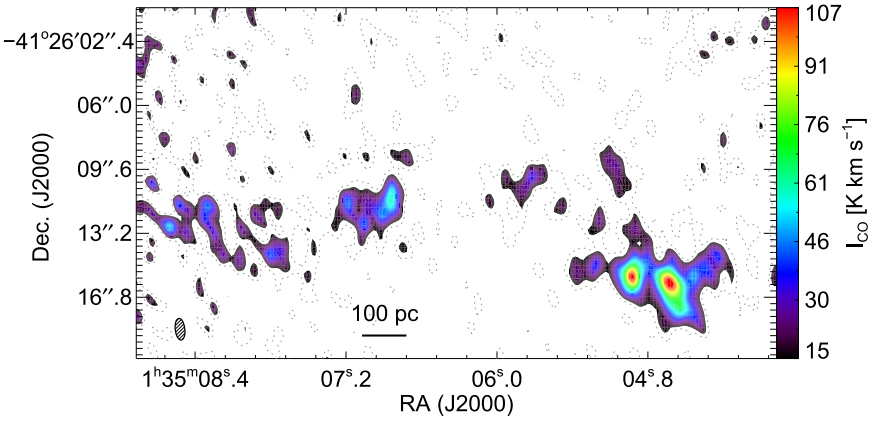

Figure 3. Total integrated intensity (zeroth moment) ALMA ^{12}CO(1–0) map of NGC 625, integrated over the velocity range 350–435 km s^{-1}. Dotted contours represent the $1\sigma_{\rm rms}$ noise level of the map, where $\sigma_{\rm rms} = 8.5$ K km s^{-1}. Range of the color scale is 2–14$\sigma_{\rm rms}$. The 1.″08 × 1.″31 synthesized beam is indicated in the lower left.

measured by Cormier et al. (2014), implying that most of the molecular gas in NGC 625 is concentrated in the nucleus of the galaxy and that our data do not miss significant extended emission.

The morphology of the molecular gas is elongated and clumpy, with the two brightest emission peaks located in the western part of the galaxy. Converting from CO luminosity, $L_{\rm CO}$, to luminous mass, $M_{\rm lum}$, requires a CO-to-H_2 conversion factor,

$$\alpha_{\rm CO} \equiv M_{\rm lum}/L_{\rm CO}. \quad (1)$$

Equivalently, $X_{\rm CO} \equiv N({\rm H_2})/I_{\rm CO}$, where $N({\rm H_2})$ is the H_2 column density. The conversion factor typically used for the Milky Way is $\alpha_{\rm CO} = 4.35\,M_\odot$ (K km s^{-1} pc^2)$^{-1}$ (Dame et al. 2001; Bolatto et al. 2013). Assuming a Galactic conversion for NGC 625, the total luminosity we measure corresponds to a total molecular mass of $(5.34 \pm 0.34) \times 10^6\,M_\odot$.

Figure A1 in the Appendix suggests that an additional third pointing in the west of the galaxy may be needed to detect all the CO emission in NGC 625. To determine whether our current ALMA observations capture the majority of the molecular gas present in NGC 625, we compare the total flux in the Herschel SPIRE 250 μm image to the flux captured within the two ALMA beams. The SPIRE 250 μm map (18″) was selected for this comparison. The Level 2 data product inferred, assuming an extended source calibration, was first background subtracted (using the median of the background flux measured within 38 apertures, with radius equal to 4 × FWHM = 72″), and then was used to measure the total flux (4.40 Jy) within a circular aperture with radius $R = 170''$, (consistent with Rémy-Ruyer et al. (2013) and their total flux measurement of 4.33 Jy). Converting the HBPW of 50.″582 to Gaussian beam sizes (with $R = 43''$), we infer a flux within the overlapping ALMA beams of 3.33 Jy, suggesting that about 76% of the total SPIRE 250 μm flux is captured within the ALMA beams. This 76% can be considered a lower limit on the CO emission that is captured within the ALMA beams, as the dust distribution is typically considered to more extended than the molecular gas in galaxies (Cortese et al. 2016).

3.2. Dynamics

In Figure 4, we display 18 velocity channel maps, each 4 km s^{-1} wide, from 360 to 395 km s^{-1}. Contour levels are multiples of the rms noise of the zeroth-moment intensity map ($\sigma_{\rm rms} = 7.61$ K km s^{-1}) displayed in Figure 3. In each channel, the contours start at $0.25\sigma_{\rm rms}$. Overplotted are the positions and position angles of GMCs identified in Section 4.2. The bulk of the molecular gas emits strongly between about 366 and 390 km s^{-1}.

A systematic velocity gradient across the galaxy is not apparent in the channel maps or in the first-moment map. We also investigated position–velocity diagrams at a number of different cuts through the data set, and found no evidence for large-scale rotation or other systematic motions (e.g., outflows) of the molecular gas in NGC 625. This is interesting because Cannon et al. (2004) find observational evidence that the complex velocity structure of the H I (at a resolution of ∼6″) is a signature of a large-scale outflow, overlapping with a disk undergoing solid-body rotation. If, as Cannon et al. (2004) suggest, the H I blowout is due to a prolonged, widespread star formation episode that has delivered sufficient energy into the ISM to drive H I into the galactic halo, it seems reasonable to expect that the molecular gas would also be similarly influenced. However, we only detect CO in the disk of the galaxy and do not see clear signatures of the blowout in the CO properties.

4. GMCs in NGC 625

In the following sections, we generate a catalog of molecular clouds in NGC 625, calculate their properties, and examine empirical relationships from their derived properties.

4.1. GMC Identification

We used the `CPROPS` algorithm (Rosolowsky & Leroy 2006) to find clouds in our 1″ data cube and measure their properties. `CPROPS` has been described in detail in Rosolowsky & Leroy (2006) and has been discussed in several recent studies that used the package (e.g., Colombo et al. 2014; Kepley et al. 2016; Faesi et al. 2018). In the following, we briefly summarize the algorithm and the parameters we chose to create the NGC 625 cloud catalog.

`CPROPS` begins by defining regions of significant emission within a three-dimensional data cube, by identifying pairs of adjacent pixels with signal-to-noise above some threshold level $t\sigma$, where σ is the rms noise level per channel. These regions are expanded to include all adjacent pixels down to a lower

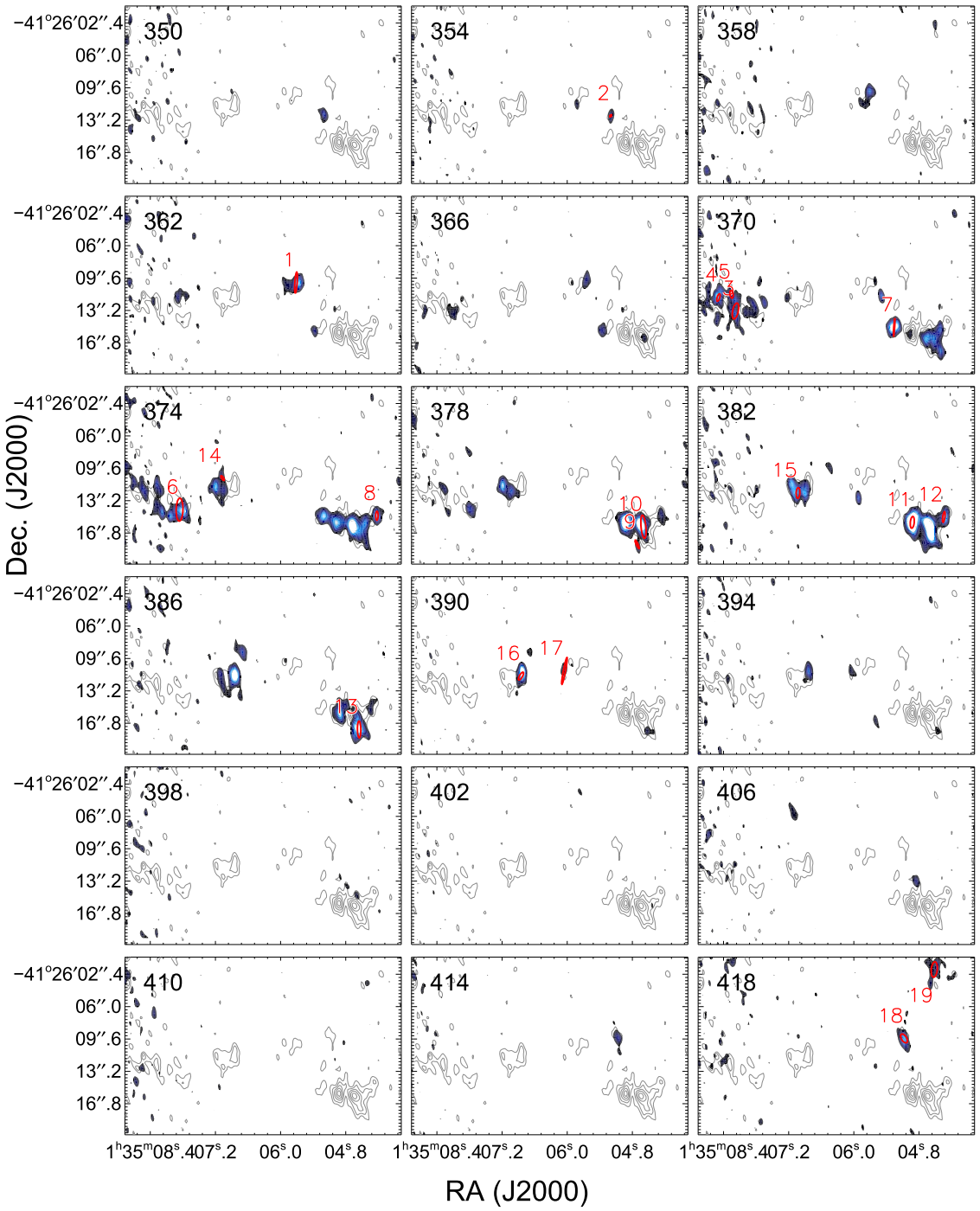

Figure 4. ALMA ^{12}CO channel maps with velocity widths of 4 km s^{-1}, shown in color. Color scale goes from $0.5\sigma_{\rm rms}$ to $2.25\sigma_{\rm rms}$, where $\sigma_{\rm rms} = 8.5$ K km s^{-1} is the rms noise level of the intensity map of the entire galaxy, integrated over the full velocity range. For context, the contour map shows the structure of the entire galaxy integrated over all velocities.

threshold level $e\sigma$. We adopted the default values, $t = 4$ and $e = 2$, similar to previous studies. Next, the algorithm identifies "islands" of emission within these regions that have an area of at least one telescope beam and that include at least two consecutive velocity channels. Finally, structures resembling molecular clouds are identified from within these islands. CPROPS searches for local emission peaks by scanning the islands with a moving box having dimensions 15 pc × 15 pc × 2 km s^{-1}. Individual clouds are picked out as objects that are above at least 2σ the shared contour with any neighboring maxima. In addition to the standard, default parameters, we used the modified CLUMPFIND (Williams et al. 1994) parameter, which requires that all detected emission is assigned to a detected cloud.

To minimize observational bias due to limited sensitivity, CPROPS extrapolates the measurements of cloud properties down to what is expected for finite sensitivity. This results in extrapolated spatial moments along the major and minor axes of the cloud, $\sigma_{\rm maj,min}(0\,{\rm K})$, and along the velocity axis, $\sigma_v(0\,{\rm K})$. Additionally, CPROPS makes corrections to account for finite

Table 3
Properties of NGC 625 GMCs

Cloud	R.A. (J2000)	Decl.	v_0 (km s^{-1})	R (pc)	σ_v (km s^{-1})	$M_{\rm lum}$ ($10^5 M_\odot$)	$M_{\rm vir}$ ($10^5 M_\odot$)	$T_{\rm max}$ (K)
1	01:35:05.72	−41:26:10.1	364.6	22.2 ± 2.7	3.2 ± 0.5	2.5 ± 0.1	2.4 ± 0.7	4.5
2	01:35:05.20	−41:26:12.7	354.5	4.3 ± 6.3	2.6 ± 0.5	0.8 ± 0.1	0.3 ± 0.6	3.8
3	01:35:08.18	−41:26:13.3	372.2	30.2 ± 7.6	3.0 ± 0.9	1.7 ± 0.5	2.9 ± 1.9	3.5
4	01:35:08.49	−41:26:11.8	373.7	14.3 ± 5.1	2.1 ± 0.8	1.4 ± 0.3	0.7 ± 0.5	4.9
5	01:35:08.25	−41:26:11.4	373.5	15.9 ± 6.0	1.8 ± 0.7	0.9 ± 0.3	0.5 ± 0.5	3.7
6	01:35:07.86	−41:26:14.2	376.2	39.6 ± 4.3	2.8 ± 0.3	3.5 ± 0.3	3.2 ± 0.9	6.4
7	01:35:05.26	−41:26:15.1	372.8	12.8 ± 1.9	4.1 ± 0.4	3.1 ± 0.3	2.2 ± 0.6	6.7
8	01:35:04.23	−41:26:14.9	377.9	14.7 ± 7.0	2.1 ± 0.5	1.1 ± 0.2	0.7 ± 0.5	5.5
9	01:35:04.71	−41:26:18.1	381.2	13.2 ± 4.6	2.9 ± 0.8	0.8 ± 0.2	1.2 ± 0.8	2.9
10	01:35:04.60	−41:26:16.1	378.4	33.4 ± 3.1	5.1 ± 0.3	10.3 ± 0.6	8.9 ± 1.3	9.9
11	01:35:04.92	−41:26:15.6	382.5	21.4 ± 2.8	4.0 ± 0.3	7.4 ± 0.5	3.6 ± 0.8	11.8
12	01:35:04.34	−41:26:15.0	384.6	15.3 ± 6.0	2.3 ± 0.4	1.4 ± 0.1	0.8 ± 0.6	4.3
13	01:35:04.55	−41:26:17.5	387.0	23.8 ± 3.4	3.8 ± 0.5	3.9 ± 0.3	3.6 ± 1.0	5.9
14	01:35:07.07	−41:26:10.7	374.7	10.4 ± 7.6	1.5 ± 0.8	0.4 ± 0.3	0.3 ± 0.3	2.4
15	01:35:07.03	−41:26:12.3	382.5	19.8 ± 3.6	4.7 ± 0.7	2.7 ± 0.3	4.6 ± 1.7	4.9
16	01:35:06.85	−41:26:11.5	390.0	16.3 ± 3.4	3.8 ± 0.5	3.7 ± 0.2	2.4 ± 0.9	8.3
17	01:35:06.05	−41:26:11.0	392.8	24.4 ± 5.1	2.1 ± 0.4	1.1 ± 0.2	1.1 ± 0.7	2.9
18	01:35:05.08	−41:26:09.5	418.5	22.8 ± 4.9	2.3 ± 0.3	1.7 ± 0.2	1.2 ± 0.4	5.3
19	01:35:04.52	−41:26:01.9	419.3	30.6 ± 8.6	1.3 ± 0.4	0.8 ± 0.2	0.5 ± 0.5	2.9

angular and velocity resolution of the data, by deconvolving the beam and channel width from measured cloud sizes and linewidths. The algorithm estimates uncertainties in cloud properties with the bootstrapping method. We used 50 bootstrap iterations to estimate the uncertainties. The extrapolation, deconvolution, and bootstrapping methods are fully explained in Rosolowsky & Leroy (2006). For further detail on how using different parameter choices in CPROPS can affect cloud properties in the final catalog, also see Faesi et al. (2018).

4.2. GMC Properties

Using the CPROPS parameters discussed above, we catalog 33 clouds. Fourteen clouds have deconvolved radii smaller than the telescope beam, and by this definition are unresolved (Rosolowsky & Leroy 2006). The remaining 19 resolved clouds make up our final catalog. Their properties are summarized in Table 3. Figure 5 displays a histogram of the peak signal-to-noise ratio (S/N) of all clouds, both resolved and unresolved. Figure 6 displays the intensity maps of individual clouds identified by CPROPS. Figure 7 shows the average ^{12}CO spectrum along the line of sight toward each cloud.

CPROPS defines the effective radius R of a cloud by subtracting the rms beam size, $\sigma_{\rm beam}$, from the extrapolated spatial moments in quadrature:

$$R = \sqrt{[\sigma^2_{\rm maj}(0\ {\rm K}) - \sigma^2_{\rm beam}]^{1/2}\,[\sigma^2_{\rm min}\,(0\ {\rm K}) - \sigma^2_{\rm beam}]^{1/2}}\,. \quad (2)$$

The one-dimensional velocity dispersion, σ_v, of a cloud is determined by deconvolving the channel width $\Delta\ V_{\rm chan}$, from the extrapolated second moment:

$$\sigma_v = \sqrt{\sigma^2_v(0\ {\rm K}) - \frac{\Delta V^2_{\rm chan}}{2\pi}}\,. \quad (3)$$

We will refer to the one-dimensional velocity dispersion and the linewidth ($\sigma_v = \Delta V_{\rm FWHM}/2.355$) interchangeably throughout the paper.

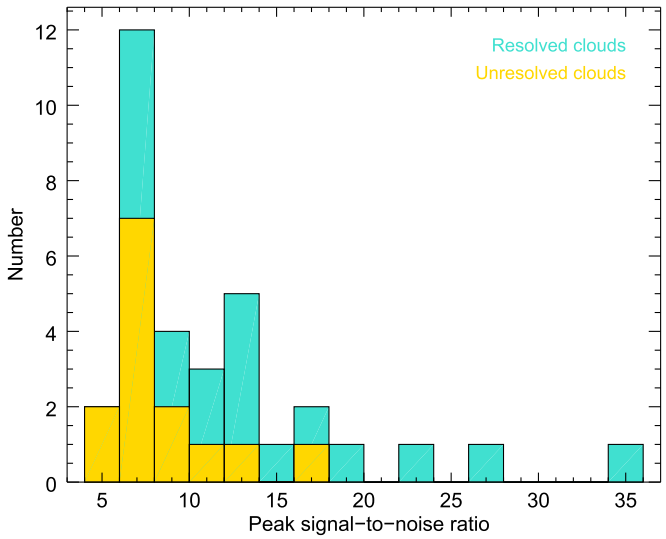

Figure 5. Histogram of the peak S/N of GMCs. Turquoise and yellow bars represent resolved and unresolved clouds, respectively.

The CO luminosity $L_{\rm CO}$, virial mass, luminous mass, and surface density are calculated as follows:

$$M_{\rm vir} = 1040 R\sigma^2_v, \quad (4)$$

$$M_{\rm lum} = \alpha_{\rm CO} L_{\rm CO}, \quad (5)$$

$$\Sigma = \frac{M_{\rm lum}}{\pi R^2}, \quad (6)$$

where R and σ_v are in units of parsecs and km s^{-1}, and assuming the accepted Milky Way value for the CO-to-H_2 conversion factor, $\alpha_{\rm CO}$. Since our knowledge of the actual CO-to-H_2 conversion factor in NGC 625 is incomplete (see Sections 4.3.2 and 6.1), we emphasize that the luminous masses we derive correspond to the CO-emitting regions of GMCs. The coefficient in Equation (5) for $M_{\rm vir}$ assumes that clouds are spherically symmetric and have power-law volume

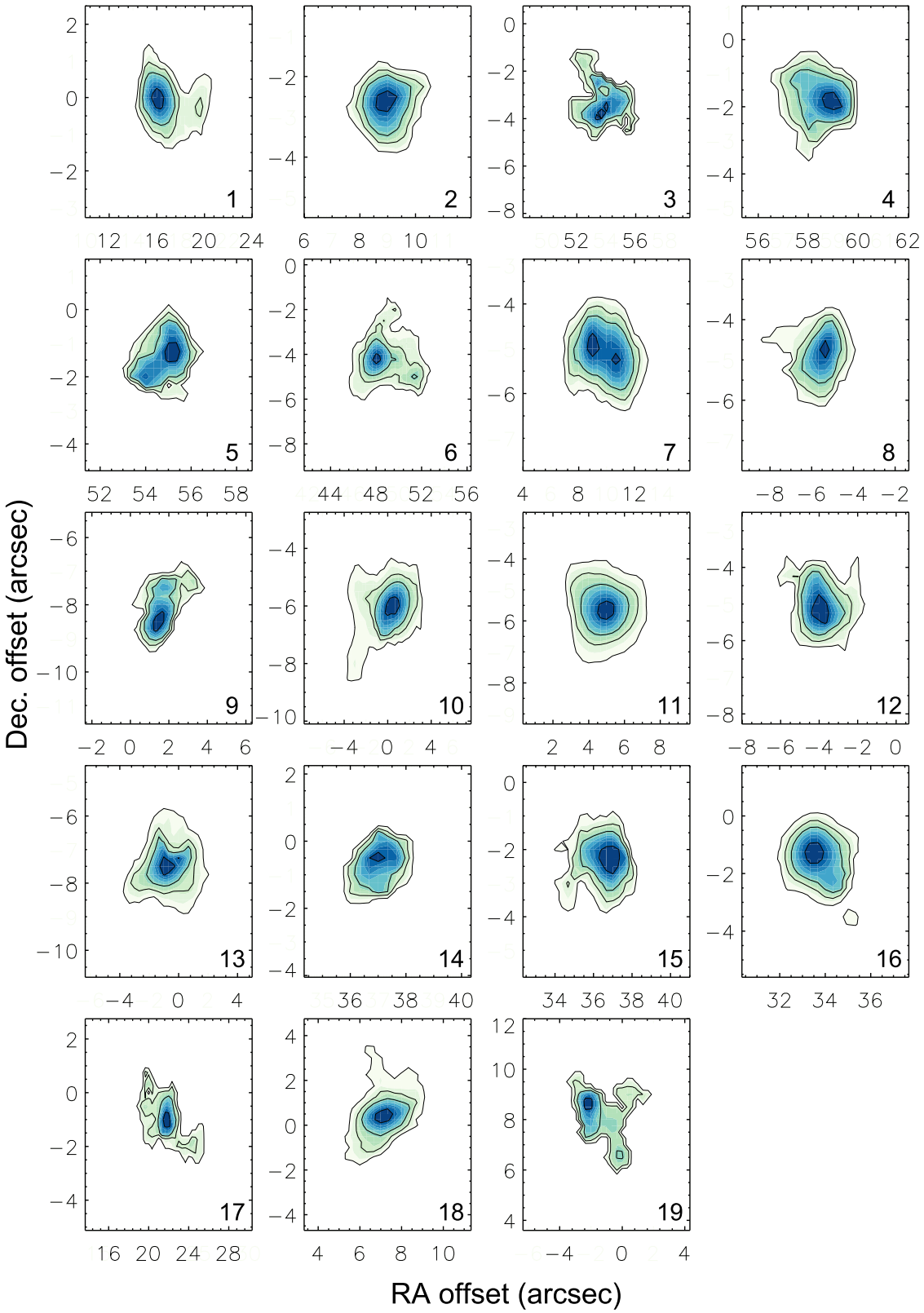

Figure 6. Integrated intensity maps of individual GMCs in NGC 625. For each GMC, the contour levels go from 10% to 90% of the peak emission of the cloud. Axes indicate the angular distance between the center of the cloud and the optical center of the galaxy.

density (ρ) profile $\rho \propto R^{-1}$ (Solomon et al. 1987; Bolatto et al. 2008).

The median values for the size, linewidth, luminous mass, and surface density of the GMCs are 20 pc, 2.5 km s^{-1}, $1.7 \times 10^5\ M_\odot$, and 169 $M_\odot$ pc^{-2}. The properties of all clouds are listed in Table 3.

Following Faesi et al. (2018), who in their study of NGC 300 molecular clouds found that GMC sizes smaller than half

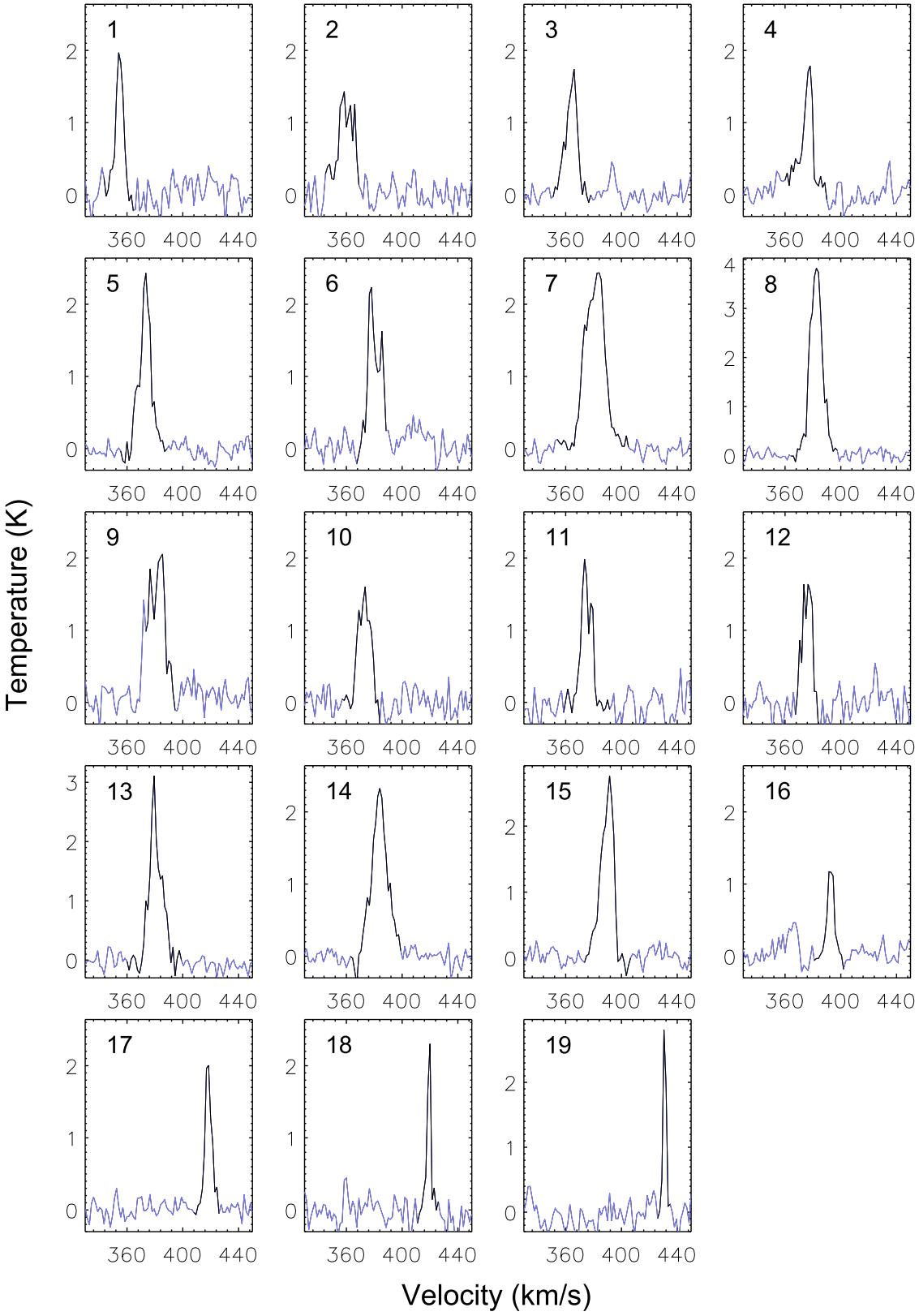

Figure 7. The ^{12}CO spectra of individual GMCs in NGC 625. For each GMC, the spectrum was generated by averaging all emission along the line of sight toward that cloud, without subtracting a velocity gradient.

the beam size were not recovered well, we adopt a resolution limit of ∼11 pc for our data. We also perform a simple test to verify that the GMCs we identify are not noise peaks. This procedure precisely follows that outlined in Appendix C of Utomo et al. (2015); see also Engargiola et al. (2003). We treat the probability of a false detection to be given by Poisson statistics, i.e., $P_n(k) = [0.5 \times \mathrm{erfc}(k/\sqrt{2}]^n$, where n is the number of adjacent channels in a cloud with signal greater than

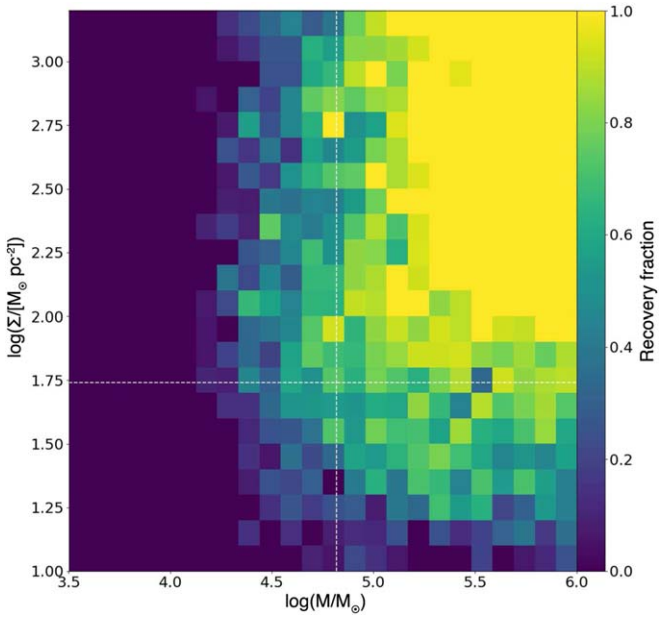

Figure 8. Illustration of the results of our completeness text. Color scale shows the recovery fraction of artificial sources as a function of mass and surface density. White dashed lines show our adopted completeness limits of $6.5 \times 10^4\,M_\odot$ and $55\,M_\odot$ pc^{-2}.

$k\sigma$, where σ is the rms noise. The probability of a real detection is then given by $1 - N_{\rm trial}P_n(k)$ for $N_{\rm trial}P_n(k) \ll 1$, where $N_{\rm trial} = N_{\rm pix}/n$ and $N_{\rm pix} \approx 7.7 \times 10^4$ is the number of pixels in the cube. Since the EDGE parameter in CPROPS is set to 2, $k = 2$ in the above. For $n = 4$, the probability of a real detection is thus 0.92, and for $n = 5$ it is 0.996. The resolved cloud with the fewest channels has $n = 5$, and thus it is very unlikely any of our clouds are misidentified noise peaks.

To more robustly estimate the completeness of our cloud catalog incorporating the effects of the decomposition algorithm, we have conducted a series of false-source injection and recovery tests. For each iteration, we generated a set of 6 to 10 molecular "clouds" with masses in the range $[10^{3.5}, 10^6]$ $M_\odot$, surface densities in the range [10, 2000] $M_\odot$ pc^{-2}, and virial parameters in the range $-1 < \log(\alpha_{\rm vir}) < 1$. Each parameter was independently and randomly chosen from a logarithmic distribution spanning the above ranges. The mass was converted to flux using a Milky Way CO-to-H_2 conversion factor and the distance of NGC 625, and then the flux was distributed as a three-dimensional Gaussian in position-position–velocity space according to the cloud's properties. These false sources were then placed randomly within a data cube with noise properties and dimension equivalent to those of our actual observations. We then ran CPROPS on this false-source data cube and compared the recovered cloud positions with the false-source positions. If the recovered cloud center fell within the footprint of the injected source, we considered this a successful recovery. We conducted 1000 iterations of this process, resulting in approximately 7000 false sources injected in total. We then calculate the recovery fraction as the number of correctly recovered clouds as a function of their parameters. Figure 8 shows a histogram of the recovery fraction as a function of surface density and mass, the two parameters that appear to have the largest joint impact on source recovery. We marginalize over each parameter individually to define our fiducial 50% completeness limits of $6.5 \times 10^4\,M_\odot$ and $55\,M_\odot$ pc^{-2}, noting that *both* of these quantities must be greater than these limits in order for a source to be reliably recovered in our tests.

4.3. The Larson Relations in NGC 625

We now investigate the scaling relations between cloud properties, frequently called "Larson's Laws" (Larson 1981). Millimeter observations show that Milky Way GMCs obey strong trends between size, velocity dispersion, luminosity, and virial mass (e.g., Larson 1981; Solomon et al. 1987). Observed trends for Milky Way clouds have often been used as a benchmark of comparison for extragalactic GMC populations. The first law, often referred to as the size–linewidth relation, says that the velocity dispersion of molecular clouds increases with size, according to $\sigma_v \sim R^{0.5}$, for Galactic clouds. The common interpretation of this relation is that the internal turbulence of clouds increases with cloud size. The second law states that the cloud luminous mass has a nearly one-to-one relation with virial mass, implying that clouds are in virial equilibrium. The third law says that cloud mass scales with size, such that clouds have roughly constant surface density.

In the next sections, we examine scaling relations for NGC 625 molecular clouds and compare them to the empirical relations determined by Solomon et al. (1987, hereafter S87) for GMCs in the inner Milky Way and first described by Larson (1981). We also consider trends derived for extragalactic molecular clouds by Bolatto et al. (2008, hereafter B08). For each set of scaling relations in NGC 625, we calculate the Spearman's rank correlation coefficient, r_s, to estimate the degree of correlation between the cloud properties. If none of the data values are repeated, a coefficient of $r_s = 1$ signifies a perfectly monotonically increasing function, while values close to zero indicate little or no correlation. We fit correlations using the "BCES" (bivariate, correlated errors with intrinsic scatter) method of Akritas & Bershady (1996). On each of the following plots displaying a Larson relation, we show the Spearman's coefficient as well as the derived fit, whether there is a significant correlation or not.

4.3.1. Size–Linewidth Relation

Figure 9 shows the plot of linewidth versus size for NGC 625 molecular clouds. Within the 1σ uncertainty of the fit, the distribution of clouds in σ_v–R space is consistent with observations of both Milky Way and extragalactic cloud populations. There is a considerable amount of scatter, and the Spearman's coefficient ($r_s = 0.18$) indicates that the correlation is poor. Nevertheless, the formal fit we derive is $\sigma_v \propto R^{0.91\pm0.36}$.

Most of the NGC 625 clouds have sizes, velocity dispersions, and luminous masses above the resolution and completeness limits (see Section 4.2). There are two resolved clouds with deconvolved radii below the 11 pc resolution limit (Clouds 2 and 14), and there is only one resolved cloud (19) with a deconvolved velocity dispersion less than the smoothed velocity resolution of 1.5 km s^{-1}. If we exclude these three GMCs and only fit data points with values of R and σ_v above these limits, the correlation remains poor ($r_s = 0.19$). This suggests that clouds below the completeness and resolution limits have a negligible effect on the size–linewidth relation.

Heyer et al. (2009) found a correlation between cloud mass surface density Σ and a size–linewidth coefficient, $C = \sigma_v/R^{1/2}$, in the Boston University-FCRAO Galactic Ring Survey, with a slope expected for gravitationally bound clouds

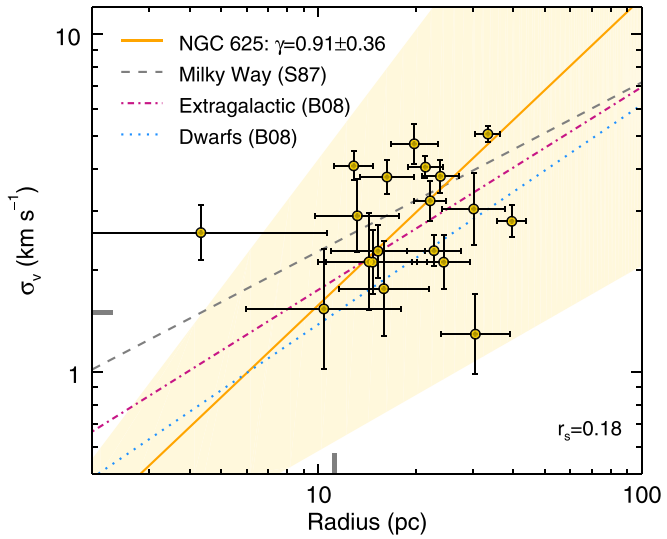

Figure 9. Size–linewidth relation for GMCs in NGC 625. Solid gold line is the fitted relation using the BCES method, with the shaded region indicating the uncertainty in the slope. Gray hatch marks indicate the estimated sensitivity limits of the observations. Spearman's rank coefficient is shown in the lower right-hand corner. Gray dashed line shows the Milky Way fit: $\sigma_v(\mathrm{km\ s^{-1}}) = 0.72R(\mathrm{pc})^{0.5}$ (S87). Pink line shows the fit for nearby galaxies: $\sigma_v(\mathrm{km\ s^{-1}}) = 0.44R(\mathrm{pc})^{0.6}$ (B08). Blue dotted line shows the fit for nearby dwarf galaxies only: $\sigma_v(\mathrm{km\ s^{-1}}) = 0.31R(\mathrm{pc})^{0.65}$ (B08).

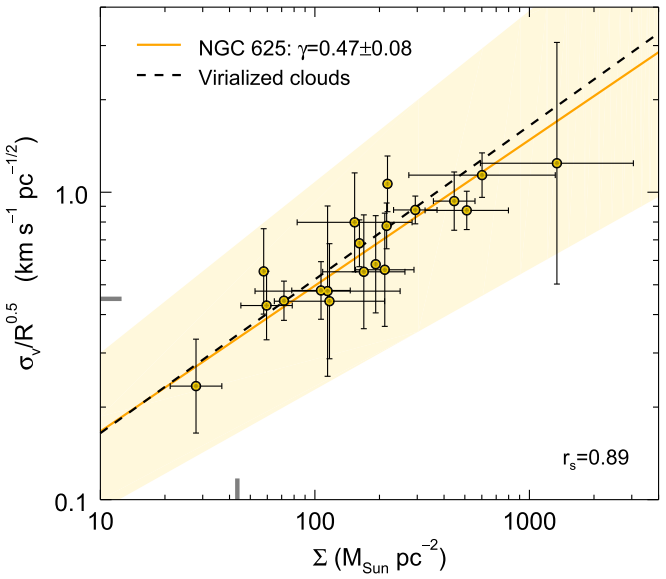

Figure 10. Size–linewidth coefficient vs. cloud surface density for NGC 625. Solid gold line is the fitted relation using the BCES method, with the shaded region indicating the uncertainty in the slope. Gray hatch marks indicate the estimated sensitivity limits of the observations. Spearman's rank coefficient is shown in the lower right-hand corner. Dashed line is the expected relation for virialized clouds.

corresponding to $\sigma_v/R^{1/2} = (\pi G/5)^{1/2}\Sigma^{1/2}$. The C–Σ plane succinctly encapsulates the Larson's relations. If all clouds in a system strictly obeyed all three Larson laws, following a size–linewidth relation with the same scaling coefficient and with identical surface densities, this would manifest as a single point located at $\sigma_v/R^{1/2} = (\pi G/5)^{1/2}\Sigma^{1/2}$. In practice, the presence of observational uncertainties would yield a cluster of points around this location.

Figure 10 shows that NGC 625 GMCs have a tight correlation between C and Σ, with a Spearman's coefficient of 0.89 and a best-fit slope of 0.47 ± 0.08, which is within 1σ of the prediction for virialized clouds shown by the dashed line, $(\pi G/5)^{1/2}\Sigma^{1/2} = \sigma_v/R^{1/2}$ (Heyer et al. 2009). We note that only one cloud has Σ less than the 50% completeness limit of 55 $M_\odot$ pc^{-2} (Cloud 19). Furthermore, only Clouds 5, 6, 17, and 19 have values of $C < 0.45$ km s^{-1} pc$^{-1/2}$, the sensitivity limit we derive for C using our resolution and spectral limits for σ_v and R defined above. If we only consider the 15 clouds above the completeness limits, we find that the linear trend is robust, with $r_s = 0.86$ and $C \sim \Sigma^{0.37\pm0.1}$.

This trend implies that the velocity dispersion of clouds does not depend uniquely on the size of the emitting region, but upon surface density as well. The correlation also suggests that the gravitational and kinetic energy of the molecular clouds in NGC 625 are in balance for surface densities spanning an order of magnitude. The C–Σ correlation emerges naturally when Σ is derived from virial masses, since $M_{\rm vir}/\pi R^2 \propto \sigma_v^2/R$. However, Heyer et al. (2009) calculated LTE-derived masses using ^{13}CO observations to measure Σ. Furthermore, it is notable that the C–Σ correlation persists when Σ is estimated from $M_{\rm lum}$, which assumes a CO-to-H_2 conversion factor, as in the case with NGC 625 and other extragalactic studies of GMCs (e.g., Bolatto et al. 2008; Faesi et al. 2018; Imara & Faesi 2019). Considering the appearance of these trends within independent data sets, Heyer et al. (2009) argued that this evidence is compatible with clouds being in virial equilibrium,

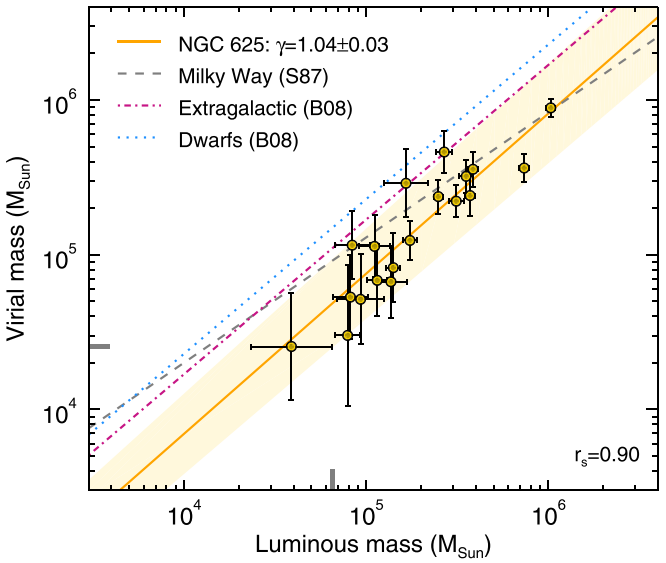

Figure 11. Virial mass vs. luminous mass for NGC 625 GMCs. Solid gold line is the fitted relation using the BCES method, with the shaded region indicating the uncertainty in the slope. Gray hatch marks indicate the estimated sensitivity limits of the observations. Spearman's rank coefficient is shown in the lower right-hand corner. Gray dashed line shows the Milky Way fit: $M_{\rm vir} = 11.5M_{\rm lum}^{0.81}$ (S87). Pink line shows the fit for nearby galaxies: $M_{\rm vir} = 2.2M_{\rm lum}^{1.0}$ (B08). Blue dotted line shows the fit for nearby dwarf galaxies only: $M_{\rm vir} = 3.0M_{\rm lum}^{1.0}$ (B08).

and that this is strong proof that the velocity dispersion in molecular clouds depends both upon the area of emission (i.e., their size) and their mass surface density.

4.3.2. Virial Relation

Figure 11 shows that there is a strong linear trend between the virial and luminous masses of GMCs in NGC 625, with a correlation coefficient of $r_s = 0.90$. We derive a fit of $M_{\rm vir} = (0.50 \pm 0.16)M_{\rm lum}^{1.04\pm0.03}$, for all 19 resolved clouds.

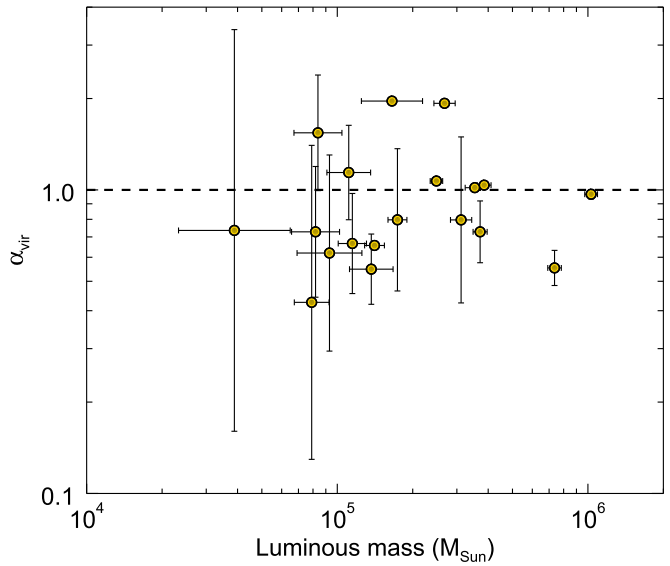

Figure 12. Virial parameter as a function of luminous mass.

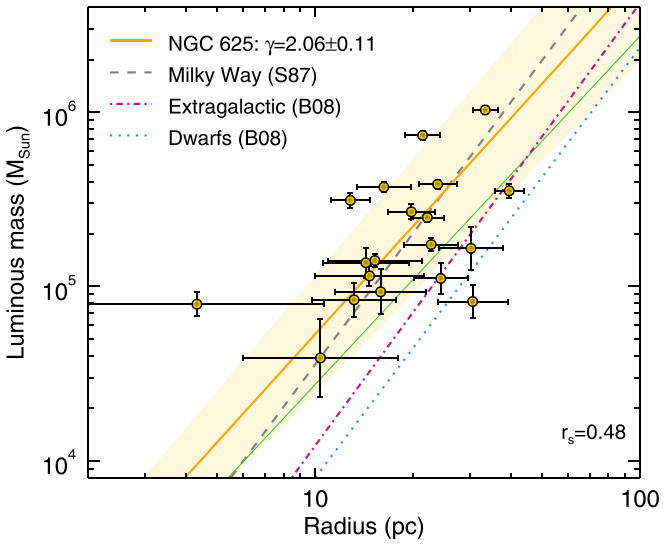

Figure 13. Mass–size relation for GMCs in NGC 625. Solid gold line is the fitted relation using the BCES method, with the shaded region indicating the uncertainty in the slope. Spearman's rank coefficient is shown in the lower right-hand corner. Green line shows the estimated sensitivity limit for constant mass surface density. Gray dashed line shows the Milky Way fit: $M_{\rm lum} = 112.5R^{2.5}$ (Solomon et al. 1987). Pink line shows the fit for nearby galaxies: $M_{\rm lum} = 35.1R^{2.54}$ (Bolatto et al. 2008). Blue dotted line shows the fit for nearby dwarf galaxies only: $M_{\rm lum} = 27.0R^{2.47}$ (Bolatto et al. 2008).

(Only Cloud 14 has virial and luminous masses below the completeness limits.)

A (nearly) linear correlation has been noticed in several previous studies of Galactic and extragalactic clouds (e.g., Solomon et al. 1987; Bolatto et al. 2008; Wong et al. 2011; Faesi et al. 2018; Imara & Faesi 2019). Such a trend, as we observe in NGC 625, suggests that clouds are in virial equilibrium. A high degree of correlation between $M_{\rm vir}$ and $M_{\rm lum}$ is expected for a moderate range of CO brightness temperatures, $T_{\rm CO}$, since $M_{\rm vir} \propto R\sigma_v^2$ and if $M_{\rm lum} \propto R^2\sigma_v T_{\rm CO}$. In our case, however, the $M_{\rm lum}$, R, and σ_v we calculate are derived from moments in the CO data cube. The luminous mass for each cloud is the sum over all pixels over which the cloud is defined, while R and σ_v are themselves intensity-weighted moments of the emission distribution (see Equations (2) and (3)). Thus, $M_{\rm lum}$, R, and σ_v are correlated but not strictly proportional.

In Figure 12, we show the virial parameter, defined

$$\alpha_{\rm vir} \equiv \frac{5\sigma_v^2 R}{GM_{\rm lum}} = 1.12\frac{M_{\rm vir}}{M_{\rm lum}}, \quad (7)$$

as a function of cloud luminous mass. Assuming that the CO emission accurately traces cloud mass, the traditional interpretation is that clouds with $\alpha_{\rm vir} \sim 1$ are in virial equilibrium, while clouds with $\alpha_{\rm vir} \gg 1$ are confined by external pressure (Bertoldi & McKee 1992). We do not detect evidence suggesting that high-mass clouds tend to be more strongly bound than low-mass clouds, as Heyer et al. (2001) did for molecular clouds in the outer Galaxy and as Colombo et al. (2014) found for M51 clouds.

Of course, reliable estimates of the virial parameter and luminous mass depend on a suitable value for the CO-to-H_2 conversion factor. At subsolar metallicity, higher CO-to-H_2 conversion factors compared to the Milky Way are expected on global scales in galaxies like NGC 625 due to the photodissociation of CO and self-shielding of H_2 (e.g., Bolatto et al. 2013). However, once CO clouds are resolved, it is not clear which conversion factor should apply. Moreover, studies on resolved scales find conversion factors in agreement with the standard Galactic value within a factor of about two (e.g., Rubio et al. 1993; Hughes et al. 2013; Indebetouw et al. 2013; Schruba et al. 2017; Imara & Faesi 2019). We remind the reader that, insofar as our knowledge of the CO-to-H_2 conversion factor is incomplete, the H_2 masses and other conversion factor–dependent quantities we derive (e.g., surface density) apply to the CO-emitting regions of clouds (see Section 4.2).

4.3.3. Mass–Size Relation

Figure 13 shows that GMC mass and size are modestly correlated in NGC 625, with $r_s = 0.48$. The vertical offset of the NGC 625 best-fit line relative to the extragalactic trends shows that NGC 625 molecular clouds generally have higher surface densities than clouds in the extragalactic samples compiled by B08. On the other hand, the surface densities implied by Figure 13 for NGC 625 clouds are consistent with the typical surface densities observed for Milky Way molecular clouds.

For Milky Way GMCs, Larson (1981) identified an inverse correlation between the mean number density, n, and size of clouds, $n \sim R^{-1.1}$. Because $\Sigma \propto M/R^2 \propto nR$, this last law implies that molecular clouds have similar surface densities. The best fit for NGC 625 clouds shown in Figure 13, $M_{\rm lum} = 466R^{2.06\pm0.11}$, is consistent with constant surface density. However, previous studies have demonstrated that the slope of ~ -1 in the density–size relation measured by Larson (1981) could be an observational artifact (Kegel 1989; Scalo 1990; Ballesteros-Paredes & Mac Low 2002).

Two factors may contribute to the apparent trend. First, Kegel (1989) demonstrated that since only clouds with column densities above a certain noise limit are detected, this effectively imposes a constant column density cutoff, which produces a slope of ~ -1 in the density–size relation (or ~ 2 in

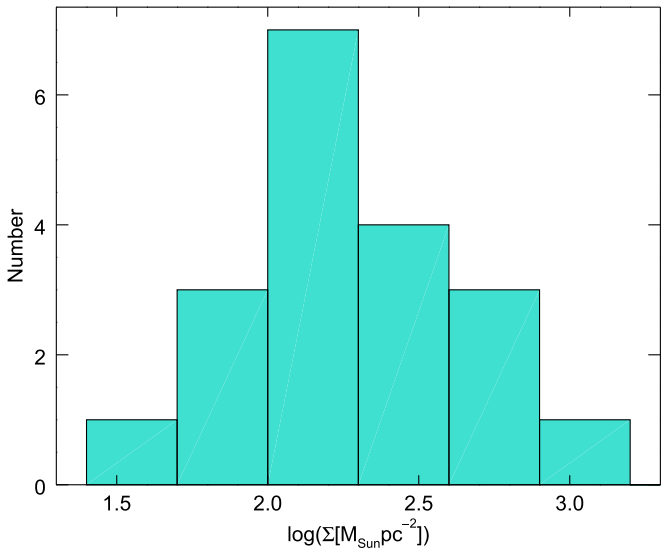

Figure 14. Histogram of GMC mass surface densities in NGC 625.

the mass–size relation). In Figure 13, we represent the line of constant mass surface density (in green) resulting from our observational sensitivity limit. Indeed, we do not detect clouds with surface densities below this threshold. If these clouds exist, it is certainly possible that they would throw off the apparent, albeit weak, trend we now observe.

A second observational artifact may be the limited dynamical range of the observations (Scalo 1990). CO observations are sensitive to a restricted range of column densities, and this can manifest as a population of clouds having roughly similar mass surface densities. The coupling of these two effects and the modest mass–size correlation ($r_s = 0.48$) in NGC 625, the $M_{\rm lum} \propto R^{2.06}$ slope should be interpreted with caution.

The considerable scatter in the mass–size distribution is also reflected in the histogram of the GMC mass surface densities presented in Figure 14. The best fit to the mass–size relation corresponds to a constant surface density of roughly 148 $M_\odot$ pc^{-2}, and the median mass surface density of NGC 625 clouds is 169 $M_\odot$ pc^{-2}, comparable to the ∼200 $M_\odot$ pc^{-2} surface density of typical GMCs in the Molecular Ring of the Galaxy (Heyer & Dame 2015). The range of values, 28–1343 $M_\odot$ pc^{-2}, spans more than an order of magnitude. Several previous studies have contended that GMCs display a wide range of surface densities in different extragalactic environments (e.g., Bolatto et al. 2008; Colombo et al. 2014; Utomo et al. 2015; Imara & Faesi 2019). In Sections 5 and 6, we explore the variety of environments occupied by clouds having various surface densities.

5. Distribution of GMCs and H II Regions

Although Wolf–Rayet signatures are detected in NGC 625, which might suggest that the galaxy is young (e.g., Schaerer et al. 1999), an analysis of its star formation history suggests an SFR that has been steadily decreasing over the past 100 Myr, with a current value of ≃0.05 $M_\odot$ yr^{-1} (Cannon et al. 2003; Skillman et al. 2003a). Star formation is mainly concentrated in the dominant H II region to the east of the galaxy, but some older events are present throughout the galaxy. There is an age gradient in the stellar population, in the sense that the youngest stars are clustered around the brightest H II regions, while the older stars (i.e., asymptotic and red-giant branch stars) are spread more diffusely throughout the galaxy (Cannon et al. 2003).

Figure 15 displays a map of Hα emission in NGC 625 observed with the HST (Cannon et al. 2003), overlaid with our ALMA CO map and the locations of GMCs. Cannon et al. (2003) cataloged the four brightest H II regions in terms of their surface brightness, calling them regions A, B, C, and D, which account for ∼95% of the total recovered Hα flux. In addition to the four brightest H II regions, Skillman et al. (2003a) cataloged several low-luminosity H II regions in NGC 625 using ground-based images. Their locations are indicated by yellow stars in Figure 15. Our new ALMA observations reveal concentrated peaks in CO emission overlapping spatially with the four regions identified by Cannon et al. (2003). We identify three GMCs each associated with region A, two with region B, one cloud associated with region C, and no clouds associated with region D.

Six clouds in all, including GMCs 1 and 14–18, are associated with the three brightest H II regions identified by Cannon et al. (2003). Five clouds—GMCs 2, 7, 9, 13, and 19—are associated with low-luminosity H II regions. The remaining eight clouds, including GMCs 3–6, 8, and 10–12, are unassociated with any prominent H II regions. We name the complex containing Clouds 3–6, to the east of H II region A, the Serpent.

The CO map reveals the presence of concentrations of molecular gas without counterparts in bright H II emission, to both the east and west of the galaxy. The largest and most massive concentration of molecular gas and clouds, located to the southwest of region C, is not associated with a high level of massive star formation activity. This concentration of molecular gas, which we have named the Butterfly (see Figure 15), is embedded with Clouds 7–12. Three of these GMCs have the highest luminous masses: Clouds 10, 11, and 13. These clouds also have the first, third, and fourth-highest virial masses, respectively.

We note that the GMCs in the Butterfly and the Serpent do not depart from the observed Larson relations in NGC 625. For instance, they are consistent with the observed $M_{\rm vir}$ $M_{\rm lum}$ trend. The GMCs in the Butterfly do have a higher average velocity dispersion, 3.5 ± 0.4 km s^{-1}, than the average σ_v of all cataloged clouds (2.4 ± 0.3 km s^{-1}). Clouds 7, 10, and 11 have three out of four of the largest one-dimensional velocity dispersions, with values > 4 km s^{-1}, in the cloud catalog. The other high-σ_v GMC is Cloud 15, associated with H II region A. In Table 4, we list the total molecular masses and surface densities of the Serpent and Butterfly

Cannon et al. (2003) found that the youngest stars in NGC 625 are predominantly located near the largest H II complexes. In their Figure 13, they compare the spatial distribution of young, massive main-sequence stars (MS; $M_V < -2.5$) with the bright H II regions, showing that the most luminous H II regions, A and B, are each associated with more than a dozen MS stars, while regions C and D are associated with far fewer. The map in Figure 13 of Cannon et al. (2003) also shows the presence of several dozen young stars located to the west of region D and north of regions A and B. (Cannon et al. (2003) do not provide the coordinates of the stars.)

What is the physical structure of molecular clouds that are (un)associated with prominent H II regions and young stars in NGC 625? For the most part, we do not detect any correlations between cloud mass, size, or velocity dispersion and the

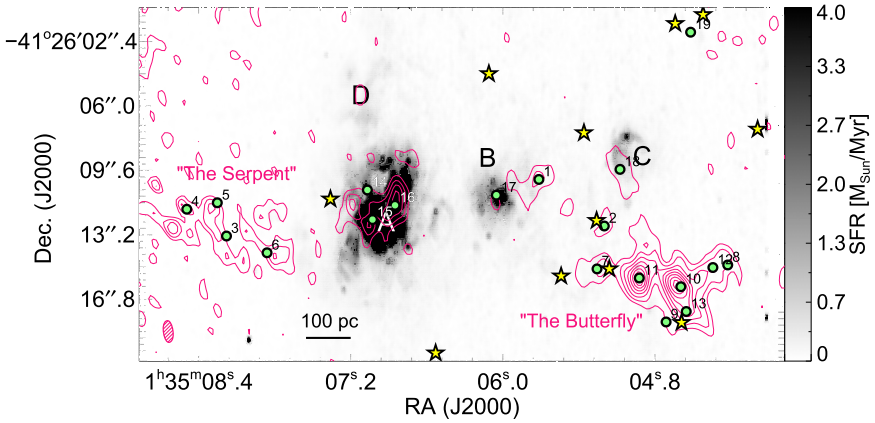

Figure 15. HST Hα image (grayscale) overlaid with the total integrated intensity ALMA ^{12}CO(1–0) map (contours) of NGC 625. Contour range of the CO map is 2–14$\sigma_{\rm rms}$, where $\sigma_{\rm rms} = 7.6$ K km s^{-1}. Green circles show the locations of GMCs identified in this paper. The four brightest H II regions are labeled A–D, following Cannon et al. (2003). Additional, low-luminosity regions identified by Skillman et al. (2003a) are shown with yellow stars. The 1.″08 × 1.″31 synthesized beam of the ALMA data is indicated in the lower left.

Table 4
SFRs and Depletion Times in Select Regions of NGC 625

Region	Size of region (arcseconds)	SFR ($M_\odot$ yr^{-1})	Total H_2 mass (10^5 $M_\odot$)	Average Σ_{H_2} ($M_\odot$ pc^{-2})	$\tau_{\rm dep}$	SFE (yr^{-1})
A	7.″2	2.0×10^{-2}	8.8	65	44 Myr	2.3×10^{-8}
B	3.″3	1.1×10^{-2}	6.8	40	62 Myr	1.6×10^{-8}
C	1.″7	7.4×10^{-4}	1.7	80	230 Myr	4.3×10^{-9}
D	1.″2	6.4×10^{-4}	0.23	65	35 Myr	2.9×10^{-8}
Butterfly	9.″5 × 4.″6	$\leqslant 5.0 \times 10^{-4}$	25	119	$\geqslant$5.0 Gyr	2.0×10^{-10}
Serpent	12.″5 × 3.″6	$\leqslant 5.0 \times 10^{-4}$	7.4	68	$\geqslant$1.5 Gyr	6.6×10^{-10}

Note. Column 1: Region name. Column 2: Either the radius or the rectangular dimensions of the region. Column 3: Average SFR. Column 4: Total H_2 mass. Column 4: Average H_2 surface density. Column 5: Depletion time. Column 6: SFE (SFE $= \tau_{\rm dep}^{-1}$).

locations of the brightest H II regions. On the other hand, we find that the highest surface density clouds are clustered in two distinct regions of the galaxy. The cloud surface density, as defined in Equation (6), ranges from 28 to 1343 $M_\odot$ pc^{-2}, with a median value of 169 $M_\odot$ pc^{-2}. Eight of the highest surface density clouds with $\Sigma > 169$ $M_\odot$ pc^{-2} are clustered in two regions of the galaxy: in H II region A (Clouds 15 and 16) and in the Butterfly (Clouds 7, 8, and 10–13). Cloud 2 has the highest surface density, with a value of 1343 $M_\odot$ pc^{-2}. If we were to define the surface density in terms of the virial mass (as opposed to $M_{\rm lum}$, as in Equation (6)), each cloud enumerated above, with the exception of Cloud 8, also has a surface density greater than the median value.

6. Molecular Gas Depletion Time in NGC 625

6.1. Global Scales

NGC 625 has a stellar mass of 3×10^8 $M_\odot$ (Madden et al. 2013) and a minimum molecular mass of 5×10^6 $M_\odot$ (Section 3.1), each more than two orders of magnitude lower than those in the Milky Way, which has stellar and molecular masses of $5.2 \times 10^{10} M_\odot$ (Licquia & Newman 2015) and 10^9 $M_\odot$ (Heyer & Dame 2015), respectively. Moreover, in NGC 625, the H I mass (10^8 $M_\odot$; Cannon et al. 2004) and SFR (0.04–0.05 $M_\odot$ yr^{-1}; Skillman et al. 2003a; Madden et al. 2013) are more than an order of magnitude smaller than in the Milky Way, which has an atomic gas mass of $8 \times 10^9 M_\odot$ (Kalberla & Kerp 2009) and an SFR of 1.65 $M_\odot$ yr^{-1} (Licquia & Newman 2015).

NGC 625 has a gas-to-stellar mass fraction, $f_g \equiv (M_{\rm H\,I} + M_{\rm H_2})/M_\star$, roughly twice that of the Milky Way. For NGC 625, $f_g \approx 0.39$, while in the Milky Way, $f_g \approx 0.17$. This result is consistent with other observations of dwarf galaxies having high gas fractions (De Vis et al. 2019). The Milky Way may have a greater proportion of its cold neutral gas in the form of molecular gas (∼11%) than NGC 625, which has at least 5% of its gas in the form of H_2. However, we repeat the caveat that the average CO-to-H_2 conversion factor in NGC 625 may be higher than the Milky Way value we assumed here to estimate the molecular gas mass (see discussion below). The global CO-to-H_2 conversion factor in NGC 625 would need to be only twice the Milky Way value—similar to the LMC (e.g., Wong et al. 2011)—in order for the galaxy to have a gas fraction on par with the Milky Way.

The molecular gas depletion timescale,

$$\tau_{\rm dep} \equiv \frac{M_{\rm H_2}}{\rm SFR}, \tag{8}$$

describes the amount of time it would take for a galaxy to use its entire supply of molecular gas at its current rate of star formation, assuming a closed system. In NGC 625, $\tau_{\rm dep} \approx 106$–134 Myr, roughly 5–6 times faster than the ∼600 Myr depletion time in the Milky Way (using the values for the molecular mass and SFR presented above), and more than an order of magnitude faster than the ∼2 Gyr depletion times measured in other nearby massive spirals (Bigiel et al. 2008).

The molecular depletion time we estimate for NGC 625 is also much faster than the 3 Gyr timescale estimated by Skillman et al. (2003a), who used the atomic gas mass to estimate $\tau_{\rm dep}$. We reiterate that this depends on the assumption of a Galactic CO-to-H_2 conversion factor. If $\alpha_{\rm CO}$ is larger in NGC 625 and the galaxy has more molecular mass than we infer here, this would imply a longer molecular depletion time. For the depletion time in NGC 625 to slow down to the ∼2 Gyr measured in massive spirals by Bigiel et al. (2008), $\alpha_{\rm CO}$ would have to be at least 10 times higher than the Galactic value. Another possibility is that our ALMA observations do not capture all of the CO emission in the galaxy (see Section 3.1).

To better constrain the global CO-to-H_2 conversion factor in NGC 625, we have estimated the conversion factor following Accurso et al. (2017), based on its scaling with the [C II]/CO ratio. Specifically, we have used Equation (26) from Accurso et al. (2017), using the (PP04) metallicity (8.36) from De Vis et al. (2019) for this galaxy and its offset from the SF main sequence, using the stellar mass measurement from Rémy-Ruyer et al. (2015) and redshift $z = 0.00132$ from NED. Based on this, we infer a global CO-to-H_2 conversion factor of 13.23 $\rm cm^{-2}$ $\rm (K\,km\,s^{-1})^{-1}$, which is three times higher than a Galactic conversion factor. We furthermore compare the observed [C II]/CO ratio ($\log$[C II]/CO = 4.028; Cormier et al. 2014) to the predicted value (3.54), using Equation (16) from Accurso et al. (2017) based on a galaxy's metallicity and offset from the SF main sequence. As the [C II]/CO ratio is known to scale with the CO-to-H_2 conversion factor, that the observed [C II]/CO ratio is larger than the predicted value suggests that the galaxy-scale CO-to-H_2 conversion in NGC 625 could be even higher than three times the Galactic value.

Given the expectation that $\alpha_{\rm CO}$ is expected to increase with decreasing metallicity (Bolatto et al. 2008; Schruba et al. 2012; Cormier et al. 2014), this is certainly plausible. Indeed, with a metallicity of $1/3Z_\odot$ (Skillman et al. 2003a), assuming that $\alpha_{\rm CO} \propto Z^{-2}$ (Schruba et al. 2012), the global CO-to-H_2 conversion factor in NGC 625 is ∼9 times the standard Galactic value.

Although the molecular gas fraction and global depletion time in NGC 625 are uncertain, what is unambiguous is that the molecular gas traced by CO and star formation are concentrated in compact regions of the galaxy. Moreover, *if* the current burst of star formation is short-lived, the galaxy will quickly run out of star-forming fuel if it is not somehow replenished quickly and if its SFR continues at its present rate. In fact, the SFR was shown to decline by a factor of ∼5 during the last 100 Myr (Cannon et al. 2003).

6.2. Small Scales

To study the molecular depletion timescale and the efficiency of star formation in individual H II regions, we compare our ALMA H_2 mass map with the resolved SFR inferred from high-resolution observations with HST (Figure 15). Based on this Hα map corrected for Galactic and internal dust extinction (Section 2.2), we infer a map of the total star formation activity in NGC 625. We note, however, that corrections for internal extinction could only be made in regions where Hβ emission was detected, toward the three brightest H II regions A, B, and C (Figure 15). Outside these regions, the inferred SFR surface density ($\Sigma_{\rm SFR}$) should be viewed as a lower limit on the true star formation activity (although, the lack of significant MIPS 24 μm emission detected outside of H II regions A and B suggest that little embedded star formation is present in those regions). To convert Hα luminosity, $L_{\rm H\alpha}$, into an SFR, $\dot{M}_\star$, we use the conversion provided by Kennicutt & Evans (2012):

$$\dot{M}_\star(M_\odot\ {\rm yr}^{-1}) = 10^{-41.27} L_{\rm H\alpha}({\rm erg\ s}^{-1}). \quad (9)$$

We average over the molecular gas mass and SFR within distinct H II regions, assuming the sizes of these regions as determined by Cannon et al. (2003). Regions A–D have diameters of 7.″2, 3.″3, 1.″7, and 1.″2, (136, 62, 32, and 23 pc), respectively. In these H II regions, the IMF has been well-sampled to infer a realistic estimate of the SFR averaged over the last 10 Myr. However, this prescription assumes a constant SFR during the last 10 Myr, which might not be applicable for NGC 625. The SFR estimates will therefore be sensitive to the average age of stars in the considered H II regions (Leroy et al. 2012).

In addition, we examine the H_2 depletion timescale in the Butterfly and the Serpent. Due to the nondetection of any diffuse Hα emission in the HST observations, we assume an upper limit of SFR $\lesssim 5 \times 10^{-4} M_\odot$ yr^{-1}, inferred from the global Hα SFR and the 10% of diffuse Hα emission missed by HST but detected in ground-based observations (Cannon et al. 2003).

The depletion times estimated from the total H_2 masses and SFRs for each region are shown in Table 4, along with the dimensions assumed for each region. We also present the molecular SFE in Table 4, which is simply the inverse of $\tau_{\rm dep}$. The depletion times associated with the four bright H II regions (A–D) range from 35 to 230 Myr, generally consistent with the globally averaged H_2 depletion timescale of 106–134 Myr for NGC 625. For the Butterfly and the Serpent, we infer lower limits on $\tau_{\rm dep}$ of $\geqslant$5.0 Gyr and $\geqslant$1.5 Gyr, which significantly exceed the typical values inferred for the H II regions. This suggests that star formation could still proceed over long timescales within the clouds in these regions. Alternatively, keeping in mind that $\tau_{\rm dep}$ is measured based on the *current* SFR, and there is no apparent star formation in these regions, perhaps star formation has yet to begin in these regions.

The differences between H_2 depletion timescales in NGC 625 at large and small scales, as well as the variations we observe between H II regions, have also been noted for regions in other galaxies (e.g., Onodera et al. 2010; Schruba et al. 2010; Liu et al. 2011; Faesi et al. 2014; Kreckel et al. 2018). Schruba et al. (2010) and Onodera et al. (2010) investigated how the CO-to-Hα ratio varies as a function of spatial scale in M33 and found a tight correlation between H_2 surface density $\Sigma_{\rm H_2}$ and SFR per unit area $\Sigma_{\rm SFR}$ on large scales ($\gtrsim$300 pc), consistent with what has been observed in previous studies (Murgia et al. 2002; Wong & Blitz 2002; Kennicutt et al. 2007; Bigiel et al. 2008; Wilson et al. 2008).

On smaller scales, however, the molecular star formation law (i.e., $\Sigma_{\rm SFR} \propto \Sigma_{\rm H_2}^n$) breaks down. Schruba et al. (2010) and Onodera et al. (2010) argued that the scale dependence of the H_2 depletion time results primarily from looking at regions in different evolutionary states. Similarly, in their study of the molecular SFE in NGC 628 at spatial scales ranging from 50 to 500 pc, Kreckel et al. (2018) demonstrated that there is an increase in scatter in the $\Sigma_{\rm SFR}$–$\Sigma_{\rm H_2}$ relation as the spatial scale decreases, suggesting that on cloud scales (∼50 pc), molecular gas and H II regions are poorly correlated. This poor correlation

may simply reflect differences in the molecular cloud properties (cloud mass, in particular) across the galaxy, as well as the different evolutionary states of the star-forming regions.

First, region-to-region differences in the properties of the molecular gas explain some of the variation in molecular depletion times observed on small scales in NGC 625. As we showed in Section 5, the surface densities and masses of GMCs in NGC 625 vary across the galaxy. Indeed, there is more than an order of magnitude range in the total molecular masses of the five regions analyzed here (Table 4), which by definition (Equation (8)) contributes to the variation in $\tau_{\rm dep}$.

The different depletion times may also reflect the different ages of GMCs. In the Milky Way and other galaxies, GMCs display a wide range of star formation activity, which stems from their varying evolutionary stages (e.g., Kawamura et al. 2009; Chen et al. 2010; Miura et al. 2010; Onodera et al. 2010). Kawamura et al. (2009) categorized GMCs in the LMC into three types, based on their association with massive star formation activity, and interpreted this as an evolutionary sequence. Those clouds with no signs of massive star formation are the youngest; those with small H II regions are currently forming stars; and those associated with both H II regions and young stars represent older clouds in the process of being disrupted by the newborn stars.

If this scenario applies in NGC 625, the molecular clouds associated with H II regions A–C may be among the oldest in the galaxy. In their stellar evolution analysis of NGC 625, Cannon et al. (2003) demonstrated that the youngest stars in the galaxy are associated with the brightest H II regions and argued that a previous star formation episode occurred around 50–100 Myr ago. In addition to the lack of bright Hα emission, the absence of any recent star formation in the Serpent and the Butterfly has been confirmed by mid-infrared Spitzer MIPS24 observations (see Figure A4, in the Appendix), which suggests that star formation has yet to commence in these parts of the galaxy. In this context, the molecular clouds in the Serpent and the Butterfly may be the youngest and are just beginning to form the next generation of stars.

7. Summary

We present new ^{12}CO ALMA observations of the dwarf starburst galaxy, NGC 625. These are the highest-resolution (1″) observations of molecular gas in this galaxy to date. We used these data to map the spatial and kinematic structure of the molecular ISM and explore the properties of GMCs in NGC 625. We summarize our results as follows:

1. The CO line is detected with high signal-to-noise in multiple locations of the galaxy. We reach an rms of 10.3 mJy per 1.5 km s^{-1} channel and report a total luminosity of 1.2×10^6 K km s^{-1} pc^2 and a molecular gas mass of at least 5.3×10^6 $M_\odot$, assuming a Galactic conversion factor. There is no ordered velocity structure.
2. CO emission is distributed in discrete clouds. Using the cloud-finding algorithm `CPROPS`, we identify 33 clouds in the map, 19 of which are resolved. NGC 625 hosts clouds of radii in the range 4–40 pc, linewidths 1.3–5 km s^{-1}, and luminous masses of $(0.04–1) \times 10^6$ $M_\odot$. Surface densities range from 28 to 1343 $M_\odot$ pc^{-2}. Our luminous mass and surface density completeness limits derived through false-source injection a recovery tests are 6.5×10^4 $M_\odot$ and 55 $M_\odot$ pc^{-2}, respectively.
3. We investigate the Larson's scaling relations and compare cloud properties in NGC 625 to trends observed among Milky Way and extragalactic GMCs. We find that the linewidths and sizes of NGC 625 clouds are, at best, weakly correlated. Measurements of virial and luminous masses suggest that clouds are in virial equilibrium. There is a modest correlation in the mass–size relationship ($M_{\rm lum} \sim R^2$), implying that clouds have a mass surface density around 148 $M_\odot$ pc^{-2} and that GMCs in this dwarf galaxy have roughly constant surface densities, similar to what we see in massive spiral galaxies. The $M_{\rm lum} \sim R^2$ correlation should be interpreted with caution, however, since this could be due to observational effects. The actual distribution of measured surface densities has a median value of 169 $M_\odot$ pc^{-2}, comparable to the surface density of typical GMCs in the Molecular Ring of the Milky Way.
4. We compare the location of the clouds with that of bright H II regions and stars. About half of the clouds are located toward the brightest H II regions, and roughly half are located in two quiescent regions to the southwest ("the Butterfly") and to the east of the galaxy ("the Serpent").
5. The global molecular depletion time of the entire galaxy is 106–134 Myr, assuming a Milky Way CO-to-H_2 conversion factor $\alpha_{\rm CO}$. However, if $\alpha_{\rm CO}$ scales with metallicity, the depletion time may be ∼9 times higher. Star formation near the brightest H II regions is rapidly depleting local sources of gas and may be on the decline if the gas is not replenished. In the Butterfly and Serpent complexes, the depletion times are >1.5 Gyr. Clouds in these regions may be younger and could be the fuel for the next generation of stars.

This paper makes use of the following ALMA data: ADS/JAO.ALMA#2015.1.01569.S. ALMA is a partnership of ESO (representing its member states), NSF (USA), and NINS (Japan), together with NRC (Canada), NSC and ASIAA (Taiwan), and KASI (Republic of Korea), in cooperation with the Republic of Chile. The Joint ALMA Observatory is operated by ESO, AUI/NRAO, and NAOJ.

The National Radio Astronomy Observatory is a facility of the National Science Foundation operated under cooperative agreement by Associated Universities, Inc.

This work was supported by the John Harvard Distinguished Science Fellowship at Harvard University. D.C. is supported by the European Union's Horizon 2020 research and innovation program under the Marie Skłodowska-Curie grant agreement No 702622. I.D.L. gratefully acknowledges the support of the Research Foundation Flanders (FWO).

Appendix

The following figures include an optical image of NGC 625, with our observed ALMA positions indicated by circles (Figure A1); the ALMA CO(1–0) peak flux map (Figure A2); an Hα image of NGC 625 overlaid with contours of 24 μm emission observed with the Spitzer MIPS instrument (Figure A3); and a 24 μm map overlaid with contours of the total integrated intensity ALMA CO(1–0) map (Figure A4).

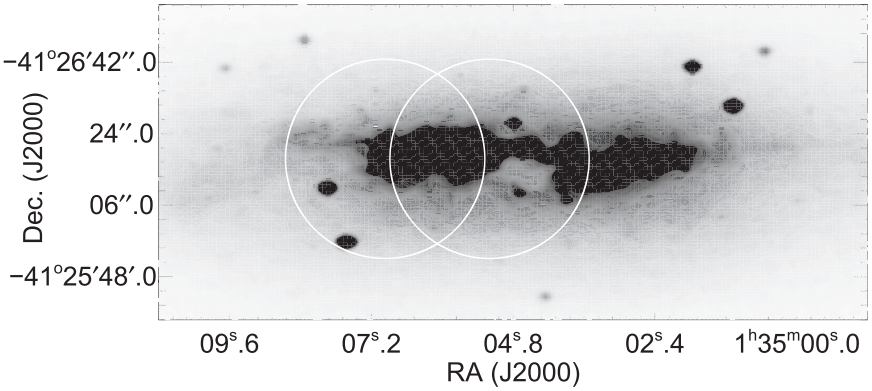

Figure A1. Optical image of NGC 625, from the CTIO 0.9 m telescope (Gallagher & Hunter 1987), overlaid with 50.″6 ALMA beams (circles).

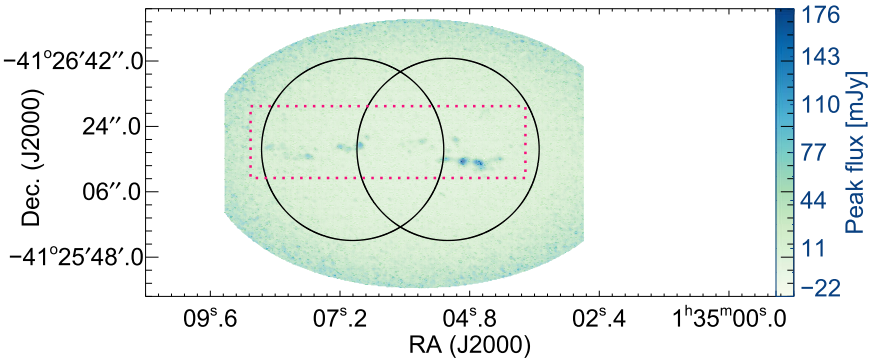

Figure A2. Map of peak flux of our ALMA observations of NGC 625. Circles represent the 50.″6 ALMA beams. White rectangle indicates the area shown in Figures 3, 4, and 15.

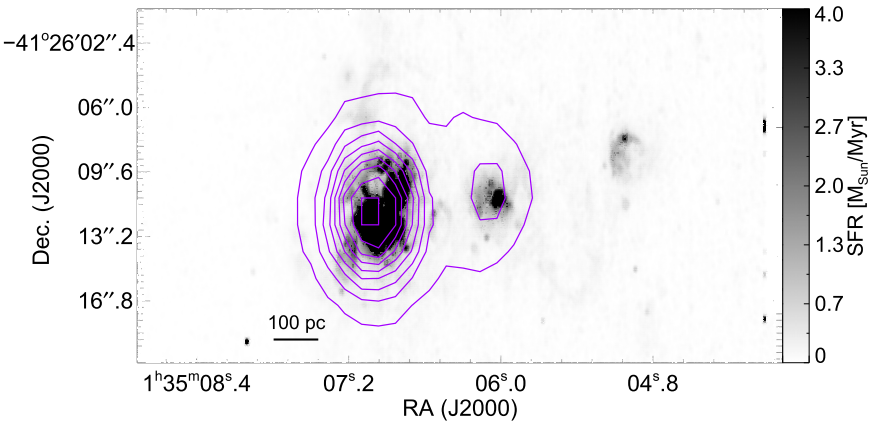

Figure A3. Hubble Hα image (grayscale), overlaid with Spitzer MIPS 24 μm map (contours; Bendo et al. 2012) of NGC 625.

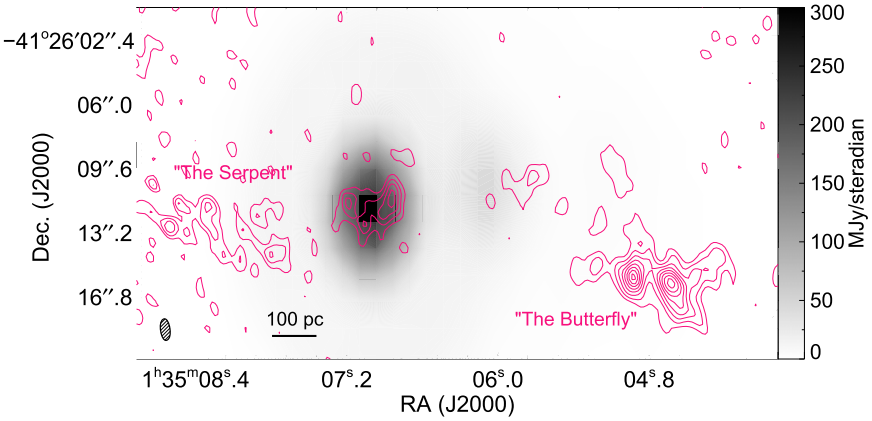

Figure A4. Spitzer MIPS 24 μm map (grayscale; Bendo et al. 2012), overlaid with the total integrated intensity ALMA ^{12}CO(1–0) map (contours) of NGC 625. Contour range of the CO map is 2–14$\sigma_{\rm rms}$, where $\sigma_{\rm rms} = 7.6$ K km s^{-1}. The 1.″08 × 1.″31 synthesized beam of the ALMA data is indicated in the lower left.

ORCID iDs

Nia Imara https://orcid.org/0000-0002-6001-598X
Diane Cormier https://orcid.org/0000-0002-1046-2685

References

Accurso, G., Saintonge, A., Catinella, B., et al. 2017, MNRAS, 470, 4750
Akritas, M. G., & Bershady, M. A. 1996, ApJ, 470, 706
Amorín, R., Muñoz-Tuñón, C., Aguerri, J. A. L., & Planesas, P. 2016, A&A, 588, A23
Arimoto, N., Sofue, Y., & Tsujimoto, T. 1996, PASJ, 48, 275
Asplund, M., Grevesse, N., Sauval, A. J., & Scott, P. 2009, ARA&A, 47, 481
Ballesteros-Paredes, J., & Mac Low, M.-M. 2002, ApJ, 570, 734
Bendo, G. J., Galliano, F., & Madden, S. C. 2012, MNRAS, 423, 197
Bertoldi, F., & McKee, C. F. 1992, ApJ, 395, 140
Bigiel, F., Leroy, A., Walter, F., et al. 2008, AJ, 136, 2846
Bolatto, A. D., Leroy, A. K., Rosolowsky, E., Walter, F., & Blitz, L. 2008, ApJ, 686, 948
Bolatto, A. D., Wolfire, M., & Leroy, A. K. 2013, ARA&A, 51, 207
Boselli, A., Lequeux, J., & Gavazzi, G. 2002, A&A, 384, 33
Cannon, J. M., Dohm-Palmer, R. C., Skillman, E. D., et al. 2003, AJ, 126, 2806
Cannon, J. M., McClure-Griffiths, N. M., Skillman, E. D., & Côté, S. 2004, ApJ, 607, 274
Cannon, J. M., Skillman, E. D., Garnett, D. R., & Dufour, R. J. 2002, ApJ, 565, 931
Cannon, J. M., Skillman, E. D., Sembach, K. R., & Bomans, D. J. 2005, ApJ, 618, 247
Chen, C. H. R., Indebetouw, R., Chu, Y.-H., et al. 2010, ApJ, 721, 1206
Colombo, D., Hughes, A., Schinnerer, E., et al. 2014, ApJ, 784, 3
Cormier, D., Madden, S. C., Lebouteiller, V., et al. 2014, A&A, 564, A121
Cortese, L., Bekki, K., Boselli, A., et al. 2016, MNRAS, 459, 3574
Dame, T. M., Hartmann, D., & Thaddeus, P. 2001, ApJ, 547, 792
de Vaucouleurs, G., de Vaucouleurs, A., Corwin, H. G., Jr., et al. 1991, Third Reference Catalogue of Bright Galaxies. Volume I: Explanations and references. Volume II: Data for Galaxies between 0$^{\rm h}$ and 12$^{\rm h}$. Volume III: Data for Galaxies between 12$^{\rm h}$ and 24$^{\rm h}$ (New York: Springer)
De Vis, P., Jones, A., Viaene, S., et al. 2019, A&A, 623, A5
Draine, B. T., Dale, D. A., Bendo, G., et al. 2007, ApJ, 663, 866
Engargiola, G., Plambeck, R. L., Rosolowsky, E., & Blitz, L. 2003, ApJS, 149, 343
Faesi, C. M., Lada, C. J., & Forbrich, J. 2018, ApJ, 857, 19
Faesi, C. M., Lada, C. J., Forbrich, J., Menten, K. M., & Bouy, H. 2014, ApJ, 789, 81
Fukui, Y., & Kawamura, A. 2010, ARA&A, 48, 547
Fukui, Y., Kawamura, A., Minamidani, T., et al. 2008, ApJS, 178, 56
Gallagher, J. S. I., & Hunter, D. A. 1987, AJ, 94, 43
Heyer, M., & Dame, T. M. 2015, ARA&A, 53, 583
Heyer, M., Krawczyk, C., Duval, J., & Jackson, J. M. 2009, ApJ, 699, 1092
Heyer, M. H., Carpenter, J. M., & Snell, R. L. 2001, ApJ, 551, 852
Hughes, A., Meidt, S. E., Schinnerer, E., et al. 2013, ApJ, 779, 44
Hunt, L. K., García-Burillo, S., Casasola, V., et al. 2015, A&A, 583, A114
Imara, N., & Blitz, L. 2007, ApJ, 662, 969
Imara, N., & Faesi, C. M. 2019, ApJ, 876, 141
Indebetouw, R., Brogan, C., Chen, C.-H. R., et al. 2013, ApJ, 774, 73
Israel, F. P. 1997, A&A, 328, 471
James, P. A., Shane, N. S., Knapen, J. H., Etherton, J., & Percival, S. M. 2005, A&A, 429, 851
Kalberla, P. M. W., & Kerp, J. 2009, ARA&A, 47, 27
Kawamura, A., Mizuno, Y., Minamidani, T., et al. 2009, ApJS, 184, 1
Kegel, W. H. 1989, A&A, 225, 517
Kennicutt, R. C., Calzetti, D., J., Walter, F., et al. 2007, ApJ, 671, 333
Kennicutt, R. C., & Evans, N. J. 2012, ARA&A, 50, 531
Kepley, A. A., Leroy, A. K., Johnson, K. E., Sandstrom, K., & Chen, C.-H. R. 2016, ApJ, 828, 50
Kreckel, K., Faesi, C., Kruijssen, J. M. D., et al. 2018, ApJL, 863, L21
Kreckel, K., Groves, B., Schinnerer, E., et al. 2013, ApJ, 771, 62
Kunth, D., & Östlin, G. 2000, A&ARv, 10, 1
Larson, R. B. 1981, MNRAS, 194, 809
Leroy, A. K., Bigiel, F., de Blok, W. J. G., et al. 2012, AJ, 144, 3
Leroy, A. K., Bolatto, A., Gordon, K., et al. 2011, ApJ, 737, 12
Leroy, A. K., Bolatto, A. D., Ostriker, E. C., et al. 2015, ApJ, 801, 25
Licquia, T. C., & Newman, J. A. 2015, ApJ, 806, 96
Liu, G., Koda, J., Calzetti, D., Fukuhara, M., & Momose, R. 2011, ApJ, 735, 63
Madden, S. C., Galliano, F., Jones, A. P., & Sauvage, M. 2006, A&A, 446, 877
Madden, S. C., Rémy-Ruyer, A., Galametz, M., et al. 2013, PASP, 125, 600
Miura, R., Okumura, S. K., Tosaki, T., et al. 2010, ApJ, 724, 1120
Miura, R. E., Espada, D., Hirota, A., et al. 2018, ApJ, 864, 120
Murgia, M., Crapsi, A., Moscadelli, L., & Gregorini, L. 2002, A&A, 385, 412
Onodera, S., Kuno, N., Tosaki, T., et al. 2010, ApJL, 722, L127
Osterbrock, D. E. 1989, PhT, 42, 123
Rémy-Ruyer, A., Madden, S. C., Galliano, F., et al. 2013, A&A, 557, A95
Rémy-Ruyer, A., Madden, S. C., Galliano, F., et al. 2015, A&A, 582, A121
Rich, J. W., de Blok, W. J. G., Cornwell, T. J., et al. 2008, AJ, 136, 2897
Rosolowsky, E., & Leroy, A. 2006, PASP, 118, 590
Rubio, M., Elmegreen, B. G., Hunter, D. A., et al. 2015, Natur, 525, 218
Rubio, M., Lequeux, J., & Boulanger, F. 1993, A&A, 271, 9
Scalo, J. 1990, in Physical Processes in Fragmentation and Star Formation, ed. R. Capuzzo-Dolcetta, C. Chiosi, & A. di Fazio (Dordrecht: Kluwer), 151
Schaerer, D., Contini, T., & Kunth, D. 1999, A&A, 341, 399
Schlegel, D. J., Finkbeiner, D. P., & Davis, M. 1998, ApJ, 500, 525
Schruba, A., Leroy, A. K., Kruijssen, J. M. D., et al. 2017, ApJ, 835, 278
Schruba, A., Leroy, A. K., Walter, F., et al. 2012, AJ, 143, 138
Schruba, A., Leroy, A. K., Walter, F., Sand Strom, K., & Rosolowsky, E. 2010, ApJ, 722, 1699
Skillman, E. D., Côté, S., & Miller, B. W. 2003a, AJ, 125, 593
Skillman, E. D., Côté, S., & Miller, B. W. 2003b, AJ, 125, 610
Solomon, P. M., Rivolo, A. R., Barrett, J., & Yahil, A. 1987, ApJ, 319, 730
Utomo, D., Blitz, L., Davis, T., et al. 2015, ApJ, 803, 16
Williams, J. P., de Geus, E. J., & Blitz, L. 1994, ApJ, 428, 693
Wilson, C. D., Petitpas, G. R., Iono, D., et al. 2008, ApJS, 178, 189
Wolfire, M. G., Hollenbach, D., & McKee, C. F. 2010, ApJ, 716, 1191
Wong, T., & Blitz, L. 2002, ApJ, 569, 157
Wong, T., Hughes, A., Ott, J., et al. 2011, ApJS, 197, 16